

The multimerization pathway of the glucocorticoid receptor

Andrea Alegre-Martí^{1,2,†}, Alba Jiménez-Panizo^{1,2,3,4,†}, Agustina L. Lafuente^{5,†}, Thomas A. Johnson³, Inés Montoya-Novoa^{1,2}, M. Nuria Peralta-Moreno⁶, Pilar Montanyà-Valluguera^{1,2}, Josep Ponsetí-Pons^{1,2}, Montserrat Abella^{1,2}, Sohyoung Kim³, Mireia Díaz⁷, Marta Vilaseca⁷, Paloma Pérez⁸, Juan Fernández-Recio⁴, Jaime Rubio-Martínez⁶, Diego M. Presman⁵, Gordon L. Hager^{3,*}, Pablo Fuentes-Prior^{1,2,*}, Eva Estébanez-Perpiñá^{1,2,*}

¹Department of Biochemistry and Molecular Biomedicine, Faculty of Biology, University of Barcelona (UB), Barcelona 08028, Spain

²Institute of Biomedicine of the University of Barcelona (IBUB), University of Barcelona (UB), Barcelona 08028, Spain

³National Cancer Institute, National Institutes of Health, Bethesda, MD 20892-5055, United States

⁴Instituto de Ciencias de la Vid y del Vino (ICVV-CSIC), Universidad de La Rioja, Gobierno de La Rioja, Logroño 26007, Spain

⁵IFIBYNE, UBA-CONICET, Universidad de Buenos Aires, Facultad de Ciencias Exactas y Naturales, Buenos Aires C1428EGA, Argentina

⁶Department of Materials Science and Physical Chemistry, Faculty of Chemistry and Institut de Recerca en Química Teòrica i Computacional of the University of Barcelona (IQTCUB), Barcelona 08028, Spain

⁷Mass Spectrometry Core Facility, Institute for Research in Biomedicine (IRB Barcelona), The Barcelona Institute of Science and Technology (BIST), Barcelona 08028, Spain

⁸Instituto de Biomedicina de Valencia (IBV-CSIC), Department of Pathology and Molecular and Cell Therapy, Valencia 46010, Spain

*To whom correspondence should be addressed. Email: evaestebanez@ub.edu

Correspondence may also be addressed to Pablo Fuentes-Prior. Email: fuentespriorpablo@gmail.com

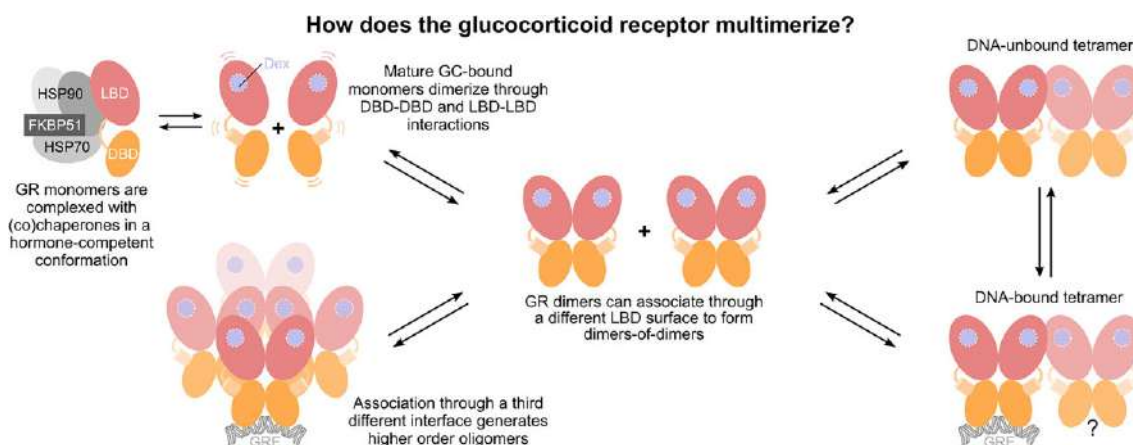
Correspondence may also be addressed to Gordon L. Hager. Email: hagerg@dce41.nci.nih.gov

†The first three authors should be regarded as Joint First Authors.

Abstract

The glucocorticoid receptor (GR) is a leading drug target due to its antiinflammatory and immunosuppressive roles. The functional oligomeric conformation of full-length GR (FL-GR), which is key for its biological activity, remains disputed. Here we present a new crystal structure of agonist-bound GR ligand-binding domain (GR-LBD) comprising eight copies of a noncanonical dimer. We verified the biological relevance of this dimer for receptor multimerization in wild-type and selected FL-GR mutants using molecular dynamics and crosslinking-mass spectrometry together with fluorescence microscopy and transcriptomic analysis in living cells. Self-association of this GR-LBD basic dimer in two mutually exclusive assemblies reveals clues for FL-GR multimerization and activity in cells. We propose a model for the structure of multidomain GR based on our new data and suggest a detailed oligomerization pathway. This model reconciles all currently available structural and functional information and provides a more comprehensive understanding of the rare disorder, generalized glucocorticoid resistance.

Graphical abstract



Introduction

The glucocorticoid receptor (GR/*NR3C1*) is a ligand-activated transcription factor essential for life [1–3]. GR belongs to the steroid receptor subfamily of nuclear receptors (NRs), which also includes the mineralocorticoid receptor (MR/*NR3C2*), the progesterone receptor (PR/*NR3C3*), the androgen receptor (AR/*NR3C4*), as well as estrogen receptors α and β (ER α /*NR3A1* and ER β /*NR3A2*) [4–6]. Full-length GR (FL-GR) shares a modular architecture with the other steroid receptors, which is crucial for their pathophysiological actions: an intrinsically disordered N-terminal domain (NTD), a highly conserved DNA-binding domain (DBD), a flexible hinge, and a mostly helical ligand-binding domain (LBD) (Supplementary Fig. S1A) [4, 6]. GR and related oxosteroid receptors (AR, PR, and MR) display a C-terminal extension named F-domain (Supplementary Fig. S1A) [6]. GR binds glucocorticoids (GCs)—such as endogenous stress hormones like cortisol or synthetic compounds like Dexamethasone (Dex)—in an internal ligand-binding pocket (LBP) [4, 7–9]. Additionally, the LBD features three solvent-exposed protein–protein binding platforms: activation function-2 (AF-2), binding function-3 (BF-3), and sensor function-3 (SF-3) [10]. These surfaces are responsible for recruiting coregulators and the chaperone/cochaperone complex (Hsp90-p23) [11–17].

NR3C1 is constitutively expressed in almost all human cells, where it mediates GC actions [2, 18, 19]. GR transcriptional activity requires binding to GC response elements (GRE) in chromatin (Supplementary Fig. S1B) [1, 3, 20–23]. Both DNA and hormone act as allosteric GR modulators that regulate receptor oligomerization [7, 24]. Ligand binding induces dimerization and docking to the DNA triggers further structural rearrangements that promote the formation of higher-order oligomers, predominantly tetramers [25], through surfaces yet to be identified. Other oxosteroid receptors have been shown to oligomerize before DNA binding [25–27]. These and other observations suggest a multi-step, highly cooperative oligomerization mechanism. Both the oligomerization state of steroid receptors, the dynamics of their interaction with chromatin and the active oligomeric conformation of the DNA-bound receptors remain areas of intense research [28–36]. Mutations in *NR3C1* are linked to human pathology, leading to either primary generalized GC resistance (PGGR), also known as Chrousos syndrome, which is characterized by the decreased sensitivity of all tissues to GCs [37–40] (Supplementary Fig. S1A) or hypersensitivity [41, 42]. GR is one of the major pharmacological targets because of its potent antiinflammatory and immunosuppressive actions, but patients on chronic GCs often develop resistance and serious side effects [43].

Structural biology has been essential in developing therapeutic GR modulators for several pathologies (e.g. asthma, psoriasis, rheumatoid arthritis, cancer, diabetes) or to prevent organ rejection [2], [43–49]. The GR-DBD homodimer has been characterized both in the absence and presence of DNA (Supplementary Fig. S1B, D, and F) [50–52]. Simultaneously, numerous crystal structures of isolated GR-LBD bound to agonists or antagonists have been reported (Supplementary Fig. S1C, E, and G) [4, 53, 54]. Recently, the structure of multidomain GR (DBD–hinge–LBD) in complex with ligand, DNA, and co-regulator peptide has been solved to medium resolution [55]. However, the hinge regions in this structure were not

defined by electron density complicating the interpretation of intra- and intermonomer contacts. Furthermore, no structure of FL-GR has been solved to date and technical limitations to assess the state of the receptor *in vivo* have stimulated intense controversy over the years [4, 53, 54]. Thus, several key questions about GR tertiary and quaternary structure remain open, including how disease-linked mutations or post-translational modifications (PTMs) affect receptor architecture [2, 6, 56, 57].

We have recently shown that GR-LBD modules can form various quaternary arrangements depending on bound agonists/antagonists and other biochemical parameters. We previously identified four GR-LBD oligomerization interfaces (termed Front, Top, Back, and Base; the first three are shown in Supplementary Fig. S1C, E, and G), the combination of which yielded a catalog of 20 topologically distinct homodimers [54]. Furthermore, our results suggested that 4 out of these 20 noncanonical GR homodimers could correspond to the transcriptionally active receptor (Supplementary Fig. S1H). On the other hand, a nonconservative replacement of a solvent-exposed residue, Asp641Val, resulted in transcriptionally compromised higher-order GR multimers, demonstrating the complexity of GR multimerization [54]. Despite these new insights, the precise pathways by which GR monomers associate to form dimers, tetramers, and/or higher-order oligomers remain unclear [25, 26]. Furthermore, since the canonical LBD dimerization mode involving parallel arrangement of H10 helices is precluded in GR and other oxosteroid receptors by the structured F-domain, the precise regions involved in receptor multimerization are still a matter of debate.

Here we present a new crystal structure of agonist-bound GR-LBD featuring an unusually large unit cell and a very high solvent content. The building block of the current structure is a homodimer whose biological relevance has been verified by crosslinking-mass spectrometry (XL-MS) and using a battery of relevant FL-GR mutants in fluorescence microscopy (Number and Brightness, N&B) experiments in living cells and RNA sequencing (RNA-seq) analysis. Several mutually exclusive assemblies of this basic dimer in the crystal highlight the versatility of GR-LBD for self-association with implications for FL-GR function in cells. We propose an alternative model of multidomain GR based on this data and suggest pathways for receptor multimerization *in vivo*.

Materials and methods

Crystallization and structure determination

Recombinant ancient multidomain GR (ancGR2–DBD–hinge–LBD) and ancGR2-LBD (corresponding to residues 416–777 and 529–777 of the human receptor, respectively) were expressed in *Escherichia coli* in the presence of 50 μ M Dex and purified to homogeneity by ion-affinity chromatography as previously described [7, 54]. Concentrated Dex-bound ancGR2-LBD was combined with a three-fold molar excess of a peptide corresponding to residues Gln18-Lys27 of the small heterodimer partner (SHP/NR0B2, box 1 motif; NH₂-QGAASRPAILYALLSSSLK-OH; Pepmic) and incubated for 1 h at room temperature. Drops of the ancGR2-LBD-SHP mixture were equilibrated at 20 °C against 0.085 M sodium cacodylate trihydrate, pH 6.5, 0.17 M ammonium sulfate, 25.5% (w/v) PEG 8000, and

15% (v/v) glycerol, using the sitting drop vapor-diffusion method.

Diffraction data to 2.78 Å resolution were collected at 100 K at the XALOC beamline of ALBA-CELLS synchrotron [58] using a PILATUS 6M detector (DECTRIS) [59] and processed using programs of the CCP4 suite (<http://www.ccp4.ac.uk/>) [60]. The crystal structure was solved by molecular replacement using MOLREP [61] and refined with REFMAC5 [62] as implemented in the CCP4 package. Global noncrystallographic symmetry (NCS) restraints were applied throughout [62]. Crystal solvent content was determined by Matthew's coefficient [63]. Crystal packing was analyzed using PISA (<http://www.ebi.ac.uk/>) [64], model quality was assessed with MolProbity (<http://molprobity.biochem.duke.edu/>) [65] and ModFOLD (<https://www.reading.ac.uk/bioinf/ModFOLD/>) [66]. Figures and videos were prepared with PyMOL (<http://www.pymol.org>).

Band-shift assays

Freshly prepared samples of multidomain GR were buffer-exchanged into 50 mM HEPES, pH 7.8, 100 mM NaCl, 10% glycerol supplemented with 1 mM ZnCl₂, 1 mM ATP and 50 μM Dex and incubated in the presence or absence of different molar ratios of a 1:1 mixture of DNA oligonucleotides comprising the GRE of *SGK1* (5'-GAAGTAATCTCTGAGAACATTTTGTCCGTTCCGCATGTAAT-3' and 5'-ATTACATGCGGAACGGACAAAATGTTCTCAGAGATTACTTC-3'). Protein-DNA complexes were separated from the individual components by native gel electrophoresis on 10% polyacrylamide gels. Gels were first stained with ultraviolet (UV) radiation after a 30-min incubation with 0.5 mg/ml ethidium bromide (EtBr) in the dark and then with Coomassie Brilliant Blue (CBB). For Western blotting (WB), one-tenth of the reaction samples were run on separate gels and then transferred overnight to nitrocellulose membranes. WB was performed using an anti-His monoclonal antibody (Abcam, 1:2000 dilution) following standard protocols.

XL-MS experiments

Samples of multidomain GR were concentrated to about 25 μM in 50 mM HEPES, pH 7.8, 100 mM NaCl, 10% glycerol, supplemented with 1 mM ZnCl₂, 1 mM ATP, 1 mM TCEP, and 50 μM Dex. Some samples were incubated for 20 min with the *SGK1* oligonucleotides at a 2:1 protein:oligonucleotide ratio prior to the crosslinking reaction. Then, crosslinkers DSSO or DSBU were added at a 50:1 molar ratio and incubated for 1 h at room temperature. The crosslinking reaction was quenched with 20 mM Tris and reaction products were separated on 10% sodium dodecyl sulphate–polyacrylamide gels.

MS experiments and analyses followed established protocols, as previously described [54, 67]. Briefly, bands corresponding to DSSO-crosslinked multidomain GR homodimers and the DSBU-crosslinked tetramers were excised from CBB-stained gels. These gel bands were washed with 50 mM NH₄HCO₃ and acetonitrile. Proteins were then reduced with 20 mM DTT at 56°C for 45 min and alkylated with 50 mM iodoacetamide at room temperature in the dark. Gel bands were washed again, and in-gel digestion was performed overnight at 37°C using 0.1 μg/μl sequencing-grade trypsin (Promega) in 50 mM NH₄HCO₃. Some samples of tetrameric GR were redigested overnight at 25°C with sequencing-grade

modified chymotrypsin (Promega) at a concentration of 0.1 μg/μl. Proteolytic digestions were stopped by adding 50 μl of 5% formic acid. Peptides were extracted first with 50 μl acetonitrile followed by 50 μl of 5% formic acid, and finally dried in a speed vacuum centrifuge (Eppendorf).

MS was performed using an Orbitrap Eclipse Tribrid mass spectrometer (Thermo Fisher Scientific) coupled to an Evosep One HPLC system (Evosep Biosystems) via a nano-Easy spray source interface. Peptides were reconstituted in 1% formic acid, 3% acetonitrile in water and separated on a 15 cm × 150 μm analytical column packed with 1.5-μm C18-beads (Evosep) at a flow rate of 0.22 μl/min. The mobile phases consisted of 0.1% formic acid in water (eluent A) and acetonitrile (eluent B). The mass spectrometer was operated in data-dependent acquisition mode. Full MS1 scans were acquired in the Orbitrap with a scan range of 375–1400 m/z and a resolution of 120 000 (at 200 m/z). Automatic gain control (AGC) was set to a target of 4 × 10⁵ with a maximum injection time of 50 ms. MS2 spectra were acquired at a resolution of 30 000 (at 200 m/z). Higher-energy collision dissociation was employed, with an AGC target of 6 × 10⁴ and a maximum injection time of 35 ms. Instrument control and data acquisition were managed using Orbitrap Eclipse Tune Application 3.5.3890 and Xcalibur version 4.5.445.18.

Searches for crosslinked peptides were conducted with MeroX [68, 69], xiSEARCH [70], and XlinkX [71] against a FASTA database comprising the GR sequence and common contaminants. We allowed for three missed cleavage sites, a minimum peptide length of four residues, and set MS1 and MS2 mass tolerances at 10 and 20 ppm, respectively. To streamline validation, an in-house script was used to merge the outputs from the three software tools. From the identified crosslinked (XL) peptides, we only considered hits plausible if they were identified with more than one crosslinking spectrum match (CSM), and preferably, if they were assigned by more than one software. The most representative CSMs were manually validated.

Cell line generation and culture

Mammary adenocarcinoma 3617-derived GR knock-out (GR-KO) cells have been previously described [72, 73]. Cells were grown in Dulbecco's modified Eagle's medium (Invitrogen) supplemented with 5 μg/ml tetracycline (Sigma), 10% fetal bovine serum (FBS; Sigma), sodium pyruvate, nonessential amino acids, and 2 mM L-glutamine maintained in a humidifier at 37°C. The FBS-supplemented medium was replaced with medium supplemented with charcoal/dextran-treated FBS to remove GCs from cells for 24 h prior to hormone treatment (100 nM Dex for 1 h). For N&B assays, cells were transiently transfected with the following variants of GFP-tagged mouse GR: wild-type (WT), Y551E, P631A, P481/P631A, P643C, Y646A, Y646A/Y722S, W718E, W718S/Y722S, and Q744A, which correspond to human mutations Y545E, P625A, P474R/P625A, P637C, Y640A, Y640A/Y716S, W712E, W712S/Y716S, and Q738A, respectively, using jetOPTIMUS™ or JetPrime reagent (PolyPlus) according to the manufacturer's instructions. The cell lines used for total RNA-seq experiments were developed in the same GR-KO cell line as previously described [72, 73]. Briefly, GFP-tagged variants of mouse GR (WT, P631A, P643A, W718E, and W718S/Y722S) were stably integrated into the GT-Rosa26 locus via CRISPR/Cas9 homology-directed repair

with puromycin selection and fluorescent-activated cell sorting. GFP-GR variants for RNA-seq and N&B were generated with the QuikChange II XL Site-Directed Mutagenesis Kit (Stratagene) or by Gene Universal.

N&B experiments and analysis

Images were taken either at the CCR, LRBGE Optical Microscopy Core facility (Bethesda, MD, USA) or at the Weber's Advance Microscopy Core (Buenos Aires, Argentina) using LSM 780 or LSM 980 laser scanning microscopes (Carl Zeiss, Inc.), respectively, both equipped with an environmental chamber. Cells were excited with a multi-line Argon laser tuned at 488 nm and imaged for 20–120 min after Dex addition using a 63 × oil immersion objective (NA = 1.4). Fluorescence was detected with a GaAsP detector in photon-counting mode.

N&B measurements were done as previously described [25, 27, 74]. For each studied cell a single-plane stack of 120 images (256 × 256 pixels) were taken with a pixel size of 80 nm and pixel dwell times of 6.27 and 8.19 μs in the LSM 780 and LSM 980 scopes, respectively. In all stacks, we discarded the first 5 images to reduce the effect of photobleaching. The frame time under these conditions is 0.97 s (LSM 780) or 1.26 s (LSM 980), which guarantees independent sampling of molecules according to previously reported fluorescence correlation spectroscopy (FCS) measurements [75]. Each stack was further analyzed using the N&B routine of the SimFCS 2.0 software (Global Dynamics), in which the average fluorescence intensity ($\langle I \rangle$) and its variance (σ^2) at each pixel of an image are determined from the intensity values obtained at the given pixel along the image stack. The apparent brightness (B) is calculated as the ratio of σ^2 to $\langle I \rangle$ while the apparent number of moving particles (N) corresponds to the ratio of $\langle I \rangle$ to B [76]. We used the SimFCS 2.0 software to classify pixels as occurring in the nucleus or the mouse mammary tumor virus (MMTV) array [77] according to their intensity values.

Cells were selected for analysis following these criteria: (i) in the case of stimulated cells, an accumulation of signal at the array must be visible, (ii) the average apparent number of molecules (N) in the nuclear compartment must have a range of 3–30 units in all cases, (iii) no saturation of the detector at any pixel ($N < 60$), and (iv) bleaching cannot exceed 5%–10%. In previous work it was demonstrated that B is equal to the real brightness ϵ of the particles plus one [76]. Therefore, ϵ at every pixel of images can be easily extracted from B measurements. Importantly, this analysis only provides information regarding the moving or fluctuating fluorescent molecules since fixed molecules (relative to our frame time) will give B values equal to 1. The experiments were independently repeated at least two times for each treatment/condition.

Total RNA collection and sequencing

RNA was isolated using the PureLink RNA kit (Thermo Fisher Scientific) following the manufacturer's instructions. We collected three biological replicates of each condition and assessed sample quality using the Agilent Bioanalyzer. Strand-specific sequencing libraries were generated from ribosomal RNA-depleted (Illumina RS-122–2301) total-RNA samples, using Illumina Stranded Total RNA (Illumina20020596) according to the manufacturer's instructions. Raw reads were demultiplexed into Fastq format allowing up to one mismatch using Illumina Bcl2fastq v2.17. Reads of the samples

were trimmed for adapters and low-quality bases using Cutadapt1.18. RNA-seq alignment to the mouse mm10 genome was performed with STAR [78]. DESEQ2 [79] was used to normalize the data by read depth, identify differentially expressed genes for each form of GR (Dex/vehicle), and calculate \log_2 fold changes (FC) and false discovery rates (FDR) for each gene.

The normalization was performed on exon reads for the entire gene using default DESEQ2 parameters. An FDR less than or equal to 0.010 and a \log_2 FC greater than or equal to the absolute value of 0.5 was used, as mentioned in the figure legends. The *P*-values reported in the comparative analysis were generated using a two-tailed, paired, nonparametric Wilcoxon signed-rank test, performed in GraphPad Prism version 10.1.1.

Docking and other bioinformatics analyses

Browser was used for superimposing structures and root mean squared deviation (RMSD) calculation (Molsoft LLC). Solvent-protected areas were calculated with PISA (<http://www.ebi.ac.uk/>). Energy terms were calculated with the bindEy module of pyDock [80]. We explored the multimerization potential of multidomain GR using pyDock docking and scoring method [80]. First, protein molecules were prepared by removing all cofactors and heteroatoms, and missing side chains were modeled with SCWRL 3.0 [81]. Then, the Fast Fourier Transform-based docking programs FTDock [82] (with electrostatics and 0.7 Å grid resolution) and ZDOCK 2.1 [83] were used to generate 10 000 and 2000 rigid-body docking poses, respectively. These were merged in a single pool for subsequent pyDock scoring, based on energy terms previously optimized for rigid-body docking. The pyDock binding energy is composed of accessible surface area-based desolvation, Coulombic electrostatics, and van der Waals (vdW) energy terms. Electrostatics and vdW contributions were limited to $-1.0/+1.0$ and 1.0 kcal/mol for each interatomic energy value, respectively, to avoid excessive penalization from possible clashes derived from the rigid-body approach.

From the resulting docking poses, normalized interface propensity (NIP) values were obtained for each residue with the built-in patch module of pyDock, implementing the pyDockNIP algorithm [84]. A NIP value of 1 indicates that the corresponding residue is involved in all predicted interfaces of the 100 lowest energy docking solutions, while a value of 0 means that it appears as expected by random chance. Finally, a negative NIP value implies that the residue appears at the low-energy docking interfaces less often than expected by random chance. Usually, residues with $NIP \geq 0.2$ are considered as part of a hotspot when using FTDock.

Molecular dynamics simulations and analysis

System preparation and molecular dynamics simulations

The crystal structure of Dex-bound human GR-LBD [Protein Data Bank (PDB) entry 4UDC] was employed to model both the WT domain and the studied mutants, Tyr545Glu, Pro625Ala, Trp712Glu, and Trp712Ser/Tyr716Ser. First, the NCOA2 peptide and CHAPS molecules were removed to generate unbound receptor conformation. Hydrogen atoms were added to all protein residues according to their protonation states at pH 7.0, and side chain orientations were optimized using the Protein Preparation Wizard from the Maestro v10.0 software suite [85]. Parameters for Dex were generated using

the General AMBER Force Field 2 (GAFF2) [86], with partial atomic charges derived using the restrained electrostatic potential method at the HF/6–31G(d, p) level [87] via the Antechamber module of AMBER22 [88]. The ff19SB AMBER force field was employed to parametrize the GR-LBD [89]. Next, the system was solvated in a cubic periodic simulation box of Optimal Point Charge water molecules, ensuring a minimum distance of 15 Å to the edges of the simulation box [90]. Water molecules within 1.0 Å of any atom in the system were removed, and counterions were added to neutralize the system using a grid-based electrostatic potential approach. A 10 Å cutoff for noncovalent interactions was applied for simulations, along with the Particle Mesh Ewald method for long-range electrostatic interactions [91]. Hydrogen mass repartitioning was introduced with ParmEd to allow integration time steps of 4 fs during the simulations [92]. The SHAKE algorithm was used to constrain hydrogen bonds [93, 94].

Before running the actual molecular dynamics (MD) simulations, and to ensure system relaxation in the unbound conformation while avoiding steric clashes, we first conducted a 20 000-steps energy minimization protocol using the steepest-descent algorithm. Then, the simulation box was heated to 300 K in 30 K increments every 20 ps by applying the Langevin thermostat algorithm under the canonical ensemble, using a collision frequency of 3 ps⁻¹, and fixing the protein backbone atoms with a 5 kcal/mol Å⁻² positional harmonic restriction. This was followed by a density equilibration protocol consisting of 200 ps of constant pressure simulation at the isothermal-isobaric ensemble, maintaining the harmonic restrictions and by a short minimization step. Finally, four independent 1 μs conventional MD replicates were performed under periodic boundary conditions in the NVT ensemble [94].

From the four 1 μs replicates, the representative structure for WT GR-LBD was obtained through clusterization using the average linkage algorithm [95] implemented in the AMBER22 CppTraj module [88, 96]. Structures visited during all the simulations were organized by similarity into 10 clusters, using the Cα RMSD as distance metric. The most populated structure was selected as the starting point for generating the 3D structures of the studied mutants. Next, MD simulations were conducted as described above for all GR-LBD mutants.

Calculation of RMSDs and root mean square fluctuations

To evaluate the structural stability of WT GR-LBD and the studied mutants along the simulation, the RMSD of each independent trajectory was computed for all Cα atoms using the CppTraj module of AMBER [96]. The minimized crystal structure of WT GR-LBD was employed as reference for all systems. For each system, all the aligned trajectories were used to compute root mean square fluctuation (RMSF) and evaluate residue fluctuations to study the backbone conformational flexibility. To characterize flexibility changes of the mutants, ΔRMSF differences were computed as:

$$\Delta\text{RMSF} = \text{RMSF}_{\text{WT}} - \text{RMSF}_{\text{mutant}}$$

Residue pair distance

To evaluate the variation of residue environment and quantify the effect of mutations on specific residue pairs, we have implemented the algorithm described by Vatansever et al. [97], essentially as previously described [67]. The algorithm ex-

tends the concept of a first coordination shell defined in the Gaussian network model to a second coordination shell (SCS), to account for nonbonded neighbor residue pairs. Briefly, for each protein residue, the time-averaged Cα, i – Cα, j distance to any neighbor in its SCS (\bar{R}_{ij}) was calculated, using a radius of ~9.1 Å to define the SCS [98]. To evaluate the impact of the mutations, the difference between WT and mutant structures was obtained as $\Delta\bar{R}_{ij} = \bar{R}_{ij}^{\text{WT}} - \bar{R}_{ij}^{\text{mutant}}$. As a global measure of the conformational changes around each residue, the average distance to all residues within its SCS was calculated according to the following equation:

$$\langle \Delta\bar{R}_i \rangle = \frac{\sum_{j=1}^N \Delta\bar{R}_{ij}}{N}$$

Time evolution and pairwise residue distances

Residue pairs exhibiting the largest structural distortions were further analyzed by evaluating their pairwise distance variations over the simulation time. Time evolution diagrams for each of the simulation replicas and distance distribution histograms of relevant Cα – Cα pairwise interactions were obtained with the CppTraj module of AMBER22 [96]. Representative frames corresponding to the most populated distances of each system identified from the histograms were extracted to visualize and compare the different conformational states. Additionally, pairwise interactions were represented with the PyMOL Schrödinger package [99].

Results

Tyr545-centered, parallel homodimers as the basic repeat unit of novel GR-LBD crystals with high solvent content

Using the resurrected variant of human GR, ancGR2 [7], which shows higher solubility and stability than ‘modern’ GR, we obtained a new crystal form of GR-LBD characterized by a large unit cell (orthorhombic space group P2₁2₁2 with a = 264.4, b = 265.5, c = 109.7 Å, α = β = γ = 90°), together with an unusually high solvent content (~70%), with channels that are up to 40 Å (Fig. 1A and B). As a result, the asymmetric unit (ASU) of the crystals contains 16 GR-LBD monomers, which have been alphabetically labeled from A to P (Fig. 1C and Supplementary Fig. S2). This is in contrast with the 22–26 copies that would have been expected in protein crystals with the typical solvent content of ~50% (see Supplementary Table S1 for a summary of data collection and refinement statistics). The unusually high solvent content likely minimized crystal packing effects, thereby favoring more physiologically relevant intermonomer contacts, as discussed below. The 16 crystallographically independent monomers can be organized into two different settings of the ASU (Fig. 1A and C). These two settings will be examined in detail below in connection with the identification of biologically relevant interfaces.

All 16 monomers feature essentially the same structure, with RMSDs that range between 0.16–0.96 Å, when only Cα atoms are considered, and 0.56–1.44 Å for all atoms. Important differences in the main chain path of the 16 independent monomers are limited to two zones located on opposite poles of the domain: the loop connecting helices H9 and H10 (L9–10) together with the N-terminal end of H10, and a surface formed by the neighboring L1–3, L6–7, and L11–12 loops (Supplementary Fig. S2A). Both main and side chains

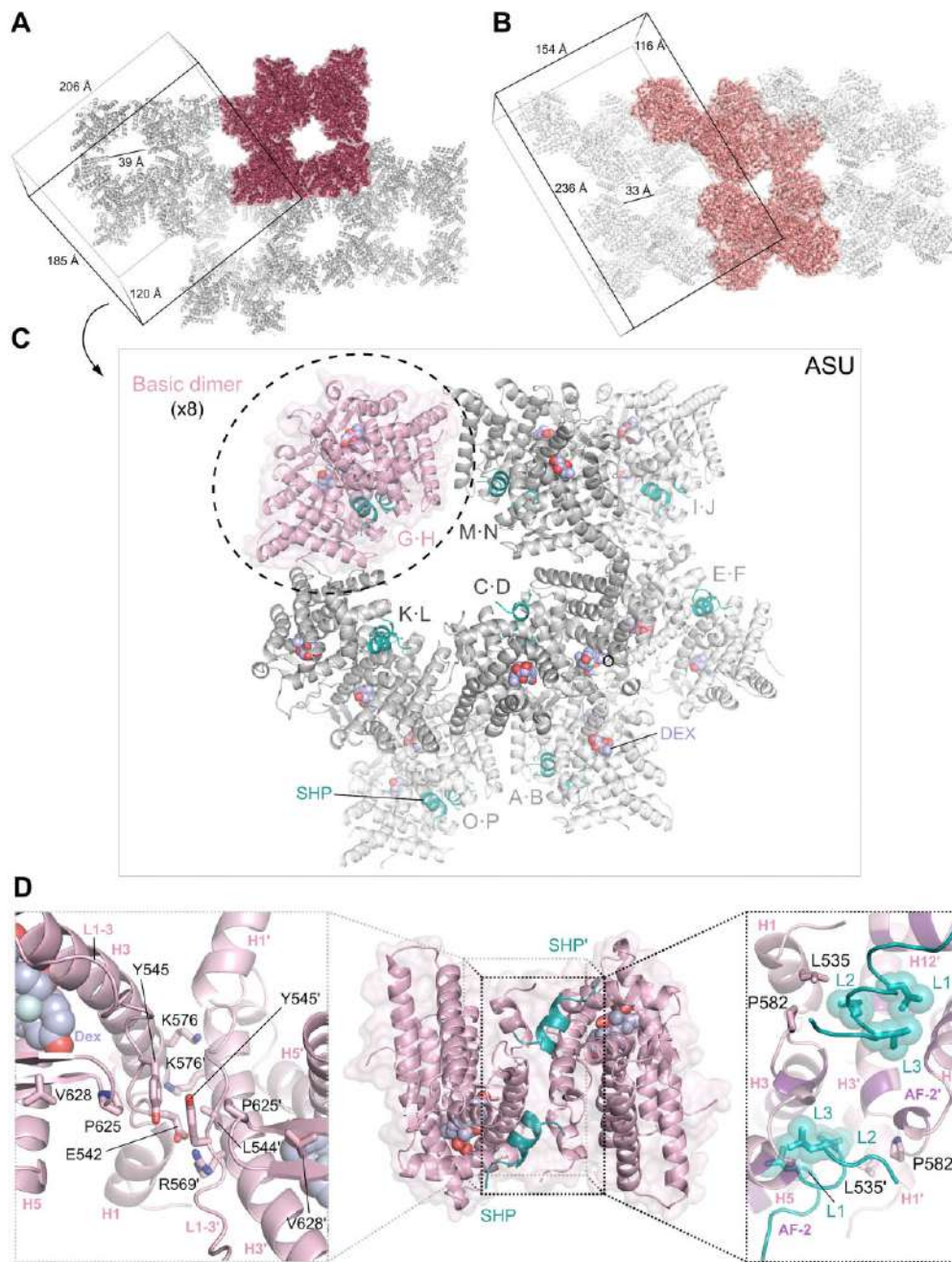


Figure 1. Novel GR-LBD crystal structure reveals the structural determinants of GR multimerization. Crystals feature an unusually high solvent content in addition to a large unit cell of about $7.7 \times 10^6 \text{ \AA}^3$, with large and wide channels filled with solvent molecules. Panels (A) and (B) depict the two different ways of choosing the ASU of the current crystals that maximize the number and quality of intermonomer contacts. These two arrangements of the 16 independent GR-LBD monomers likely capture pathophysiologically relevant protein–protein contacts *in vivo* (see main text for details). **(A)** Choice of the ASU centered on residues of helices H9/H10 and the connecting loop (L9-10). Because of the prominent role of the Trp712 indole rings in this arrangement, it will be referred to as the ‘Trp712 setting’. The 16 crystallographically independent GR-LBD monomers are colored in burgundy. (See Fig. 2 for details of intermonomer contacts in this setting). **(B)** An alternative choice of the ASU will be referred to as the ‘Pro637 setting’ as the major organizing elements are residues of the L6–7 loop, most notably Pro637. The 16 independent GR-LBD monomers are colored in coral. (See Supplementary Fig. S4 for details of intermonomer contacts in this setting). **(C)** A view of the ASU of the crystals in the Trp712 setting, with all 16 independent GR-LBD molecules represented as cartons. Note that these 16 monomers associate to form eight similar parallel homodimers, which form the basic repeating unit of the ASU. One of these basic dimers is colored pale pink and the other seven dimers are shown in different shades of gray depending on their position along the axis perpendicular to the plane of the page. Coregulator SHP peptides bound to the AF-2 cleft are shown as teal cartoon and the Dex molecule bound in the LBP is represented as light-blue spheres with red-colored oxygen atoms. **(D)** The basic GR-LBD homodimer belongs to class #6 in our catalog of possible homodimeric arrangements (Supplementary Fig. S1H) [54]. The dimer is shown as a pale pink cartoon at the center of the panel, with coregulator peptides and Dex molecules colored as in C. Close-ups of the protein–protein dimer interface are shown to the right and left. Note the central position occupied by the stacked phenol rings of residues Tyr545/Tyr545', as well as the stabilizing role of Pro625 and Val628 (left panel). (Residues from the second monomer in the basic dimers are primed). Interactions of SHP residues Leu21, Leu25 and Leu26 with the AF-2 cleft are highlighted in the right panel. (Labeled L1, L2 and L3 in the figure for simplicity). Note that the bound peptides cross-connect the two monomers: in addition to occupying the AF-2 cleft of its ‘own’ LBD in a canonical manner, the more C-terminal SHP residues contact the neighboring GR module.

of all monomers are well defined by electron density, with the only exception of monomer H in which side chain atoms are much more poorly defined due to enhanced thermal motion (Supplementary Figs S2B and C, and S3).

Most notably, the L9–10 loop adopts in several monomers a ‘closed’ conformation characterized by a Glu705–Gly706 tight turn with a solvent-pointing Glu705 side chain and H10 N-terminally extended to residue Asn707 (Supplementary Fig. S2D). We use throughout the manuscript a numbering system based on the canonical human sequence, UniProt entry P04150-1, corresponding to variant GR α -A. This doubly capped structure of H10 is similar to the path followed in the high-resolution structure of mouse GR-LBD featuring mutations Val702Ala and Glu705Gly, which lead to enhanced stability of the LBD module (PDB entry 3MNP) [100]. By contrast, residue Glu705 points towards the interhelical space in other monomers and the L9–10 loop adopts an ‘open’ conformation that is not well defined by electron density in most monomers, indicating enhanced mobility (Supplementary Figs S2E and S3A–C). Interestingly, all but one dimer (O·P) feature GR-LBD modules in which one loop L9–10 adopts the closed, while the other is found in the open conformation. This observation suggests that the flip-flop movement of residue Glu705 and the accompanying rearrangements in this region are linked to L1–3 and thus to homodimer formation, in line with the results of Seitz and coworkers [100] and previous MD simulations [101].

The 16 copies of the GR-LBD monomers are organized into eight similar, parallel homodimers that belong to class #6 as listed in our catalog of homodimeric arrangements (Supplementary Fig. S1C, D, and H) [54]. The RMSDs between the different dimers range between 0.30–0.93 Å and 0.71–4.75 Å for C α and all atoms, respectively. These ‘basic’ homodimers are generated by contacts between solvent-exposed residues in loops L1–3 and helices H3 from the two monomers (Fig. 1D). These residues are strictly conserved or conservatively replaced from fishes to humans, particularly in human GR, highlighting the biological relevance of the arrangement. At the center of this interface, the phenolic side chains of residues Tyr545/Tyr545’ stack on each other and are perfectly defined by electron density in all pairs (Fig. 1D and Supplementary Fig. S2F). This is in addition to strong salt bridges between the carboxylate of Glu542 and the guanidinium group of Arg569’ and *vice versa*, which are well protected from bulk solvent by the aliphatic side chains of Leu544’/Leu544. Disruption of these salt bridges might explain the functional impairment of the recently reported mutation linked to Chrousos syndrome, p.Arg569Gln (Supplementary Table S2) [102]. Further, the aliphatic parts of residues Lys576/Lys576’ make vdW contacts with each other and in addition engage in both vdW and electrostatic interactions with residues Ile539’/Ile539 from the neighboring monomer. Altogether, 565 ± 15 Å² are protected from bulk solvent in these parallel, Tyr545-centered homodimers (see Supplementary Table S3 for the contribution of different energy terms to dimer stability). Notably, the conformation of the Tyr545 side chain is stabilized by strong vdW interactions with Pro625, a strictly conserved residue in the underlying loop connecting H5 and H6 (Fig. 1D). Previous studies have assessed the relevance of the L5–6 loop, especially of residues Pro625 and Ile628, for GR oligomeric state and activity [4, 25, 26]. For simplicity, in the following we will refer to this local structure as the ‘Tyr545 interface’, with the un-

derstanding that other neighboring residues of the L1–3/H3 area and the underlying Pro625/Ile628 are integral elements of the interface.

Dimer-dimer contacts reveal two alternative mechanisms of oligomeric arrangements with implications for receptor multimerization in living cells

We reasoned that the high solvent content of the current crystals results in arrangements that are not imposed by crystal packing contacts and are thus likely to reproduce interactions characteristic of *bona fide* FL-GR multimers detected in living cells, as visualized in our N&B studies [25, 54]. Despite their apparent complexity, the arrangements of these GR-LBD dimers in the current crystal can be comprehensively described by two different combinations of dimer-dimer contacts, which are essentially made by the most flexible regions of the domain, the H6/L6–7/H7 area (Supplementary Fig. S4 and Supplementary Video S1, referred to as the ‘Pro637 setting’) and the H9/L9–10/H10 area (Fig. 2 and Supplementary Video S2, labeled as the ‘Trp712 setting’; see also Fig. 1A and B). These two settings not only result in different overall arrangements of the eight GR-LBD dimers in space but also turn out to have radically different functional implications, as discussed below.

An intricate network of protein–protein interactions centered on the Pro637 interface generates octameric GR-LBD assemblies

The choice of the ASU that results in a more compact packing of monomers in the crystal focuses on contacts mediated by residues of the L6–7 loop (Leu636, Pro637) and the N-terminus of H7 (e.g. Tyr640, Asp641), with additional contributions from neighboring L1–3/H3 and L11–12 residues (Supplementary Fig. S4A and Supplementary Video S1). These contacts, described in detail in the legend to Supplementary Fig. S4, generate two similar, irregular octamers, comprising monomers (A·B):(C·D):(E·F):(G·H) and (I·J):(K·L):(M·N):(O·P), with central dimers B·C and J·N, respectively. These tetramers-of-dimers can be considered to form by the initial association of two Tyr545-centered dimers, A·B and C·D, through symmetric contacts of their L6–7 loops (Supplementary Fig. S4B and Supplementary Video S1). This is followed by the docking of two additional dimers, E·F and G·H, from ‘below’ and ‘above’ onto this core dimer-of-dimers, respectively (in the orientation shown in Supplementary Fig. S4B). Although monomers E and H also rely on L1–3 and L6–7 for protein–protein interactions (PPIs), these ‘lower’ and ‘upper’ subunits dock asymmetrically onto the central dimer-of-dimers so that they simultaneously contact both monomers B and C. The octamer is closed by minor contacts between the peripheral monomers, A·F and D·G. Altogether, 2165–2200 Å² are protected from bulk solvent at the intermonomer interfaces. Similar contacts are made by the topologically equivalent GR-LBD modules that form the second octamer, although there are large differences both at the level of relative intermonomer orientations and details of PPIs (Supplementary Fig. S4). These observations underscore the high degree of plasticity of intermonomer contacts in the current crystal. While this view of the ASU is crystallographically appealing due to its division into two topologically equivalent octamers, it is important to note that several residues of the Pro637 interface,

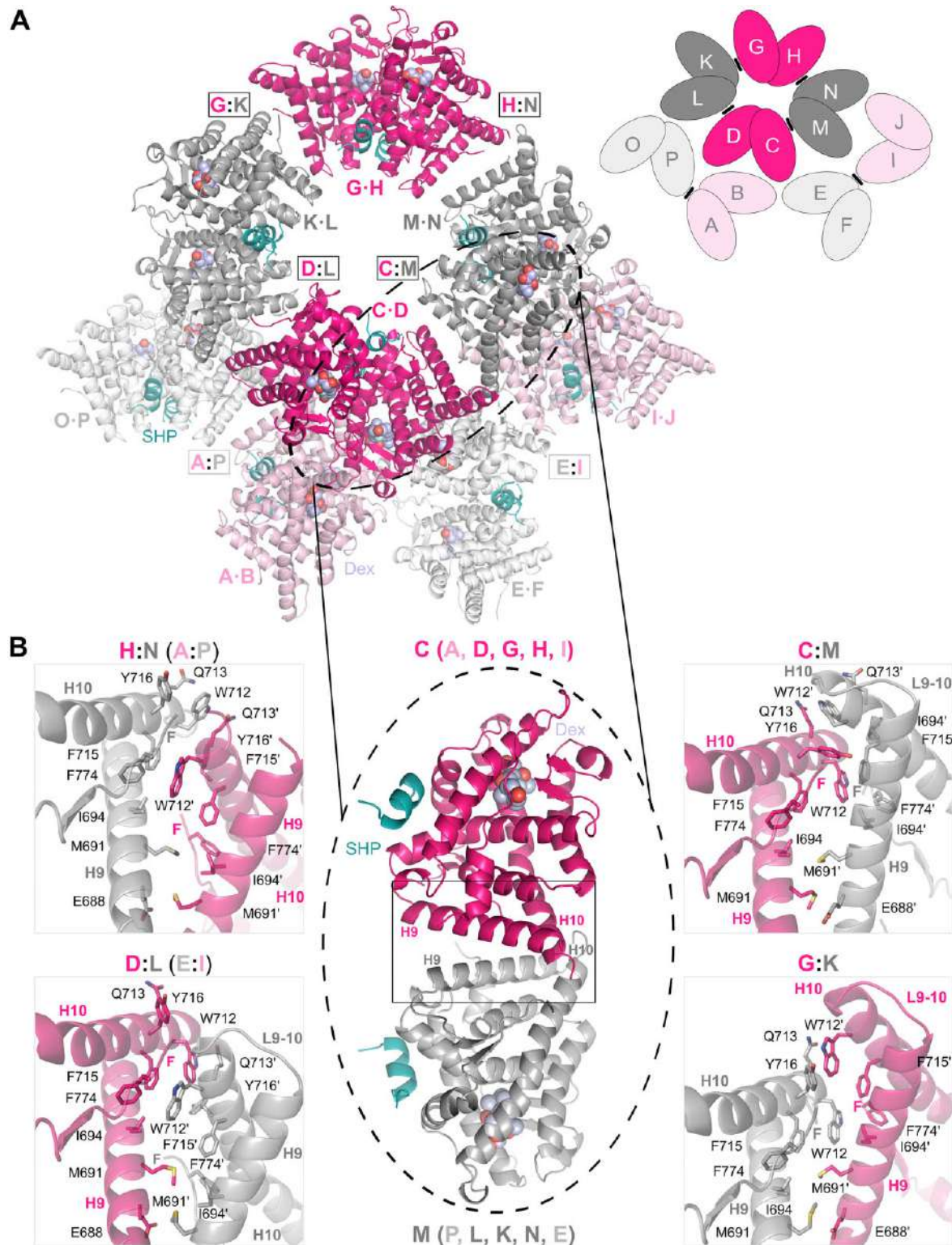


Figure 2. The Trp712 setting features six topologically equivalent dimers-of-dimers generated by contacts between aromatic residues at the N-terminus of H10. **(A)** Overall view of the eight GR-LBD homodimers in the ASU chosen to highlight dimer-dimer contacts between residues of the H9/L9–10/H10 area, the Trp712 setting. Dimers are colored according to their relative positions in the 3D structure. In the forefront, dimers C-D/G-H and K-L/M-N are colored in fuchsia and dark gray, respectively. In the background, the second layer of dimers, A-B/I-J and E-F/O-P, are colored in pale pink and light gray, respectively. The six interdimer contacts centered on the triplet of aromatic residues, Trp712/Phe715/Tyr716 (A:P, C:M, D:L, E:I, G:K, and H:N) are boxed. A schematic representation of the setting is shown in the inset to the right, with GR-LBD molecules given as ovals and contacts at the Trp712 interfaces highlighted with black bars. The SHP coregulator peptides and Dex molecules are color-coded as in Fig. 1. **(B)** Comparison between the six different arrangements of Trp712-centered dimers-of-dimers. The D-C:M-N dimer-of-dimers is shown in the central panel. (For simplicity, only the contacting monomers, C and M, are represented). Close-ups of the six interfaces are shown in the insets: A:P/H:N and E:I/D:L (to the left) as well as C:M and G:K (to the right). Major interface residues are shown as color-coded sticks and labeled. Note the central position of residues Trp712/Trp712' and the different intermonomer orientations (see also [Supplementary Video S2](#)).

especially Pro637 itself, are atypical for biologically relevant interfaces, which predominantly feature large aromatic (Phe, Tyr, Trp) or charged residues (Asp/Glu and Lys/Arg).

The Trp712 interface is a plastic, highly populated PPI surface

Six of the protein–protein interfaces in the current crystal structure involve residues of helix H9, the N-terminus of H10, and the connecting L9–10 loop, making it the second most common interface (Fig. 2A). The most relevant element of this interface is a strictly conserved triplet of nearby aromatic residues, Trp712, Phe715, and Tyr716, arranged around the indole rings of Trp712/Trp712' (Supplementary Video S2). For this reason, in the following we will refer to this PPI surface as the ‘Trp712 interface’. A comparison of the six Trp712 interfaces reveals common structural features. In the orientation shown in Fig. 2B, the indole ring of Trp712 from the ‘left’ GR-LBD molecule docks onto the Gln713' side chain from the ‘right’ monomer making important vdW contacts. The corresponding Trp712' side chain from this right subunit projects into an aromatic/aliphatic pocket shaped by the Ile694 (H9) and Phe715 (H10) side chains, along with the phenol ring of the C-terminal Phe774 (F-domain). This core interface is completed by additional vdW contacts between side chains of other residues in the central region of H9/H9', most notably Met691/Met691' (e.g. Met691-Glu688', Ile694-Met691'). Altogether, the H9/L9–10/H10 interfaces bury surface areas of similar magnitude as bona fide, physiologically relevant PPI interfaces [103–105] (470–750 Å²) and have large calculated binding energies (Supplementary Table S3).

Although the six Trp712 interfaces are topologically equivalent, as they are formed by the same secondary structure elements, large differences in the interdimer orientations are evident (Fig. 2B, Supplementary Fig. S5, and Supplementary Video S2). Closer inspection reveals that two of the pairs (A:P/H:N and D:L/E:I) are most closely related to each other, with an overall RMSD of about 2 Å for all C α atoms (Supplementary Table S4). (For simplicity, we will only discuss monomers interacting through their H9/L9–10/H10 regions. It is important to note, however, that these assemblies are actually formed between dimers [e.g. (A-B):(O-P), (H-I):(M-N), etc]). This leaves four easily distinguishable conformations of Trp712-centered dimers-of-dimers, exemplified by pairs H:N, D:L, C:M, and G:K (Fig. 2B). Even in two pairs of dimers that adopt similar relative orientations, A:P and H:N, the side chain of Tyr716' swings between a Trp712-distant and a Trp712-close conformation (Supplementary Fig. S5A). Thus, the interconversion between the different Trp712-centered assemblies of GR-LBD tetramers can be described as a ratcheting of two GR-LBD dimers relative to each other around the fixed pair of central Trp712 side chains, with additional side chain adjustments (Supplementary Fig. S5B and Supplementary Video S2). For instance, the conversion from the A:P/H:N to the G:K pose involves a large rotation of helix H9' towards Trp712. This movement allows for additional interactions of the Trp712 indole ring with Met691' (Supplementary Fig. S5C), while the Trp712' and Tyr716 side chains engage in additional contacts (Supplementary Fig. S5D).

Although not exactly superimposable on any of the current Trp712-mediated dimers, topologically equivalent arrangements of GR-LBD monomers can be identified in several pre-

viously reported crystal structures, including the first structures of the module, also bound to Dex (PDB entries 1M2Z and 1P93) [4, 53] (Supplementary Fig. S5E). This is in addition to GR-LBD complexes with the natural hormone, cortisol (4P6X) [106] or with unrelated nonsteroidal GCs (3CLD, 3E7C, and 3K22) [107–109]. Altogether, these observations underscore the high degree of plasticity at the Trp712 interface.

One important feature of these dimer-of-dimers interfaces is that the gathering of the six exposed aromatic side chains generates pockets that could be occupied by aromatic/aliphatic small molecules. In fact, extra electron densities observed in the current structure could be safely interpreted as polyethylene glycol (PEG) molecules of different lengths derived from the crystallization solution (Supplementary Fig. S2G). This adds to previous observations by us and others of small molecules bound at this solvent-exposed surface, which is adjacent to but topologically distinct from the BF-3 pocket. We have termed this GR-LBD cavity ‘SF-3’; its role in regulating GR biological activity is discussed elsewhere [10].

Tyr545-centered, noncanonical homodimers are essential for GR multimerization

The presence of eight similar Tyr545-centered GR-LBD dimers as the basic repeating unit in the current crystals strongly suggests that their formation precedes crystallization. This observation, along with our previous data showing the impact of the Y545A mutation on GR oligomerization and transcriptional activity [54], prompted us to assess in more detail its relevance in living cells. To this end, we generated a new FL-GR mutant of the central interface residue, Tyr545 (variant GR^{Y545E}), aimed at exploiting the electrostatic repulsion of approaching Glu545 side chains. In addition, we mutated a residue that makes important contacts with the phenol ring of Tyr545, Pro625 (variant GR^{P625A}) (Fig. 3A). We first confirmed comparable expression levels of WT and mutant GR variants (Supplementary Fig. S6A). Next, we studied the oligomerization behavior of these mutants by N&B, both in the nucleoplasm and at the MMTV array (Fig. 3B and Supplementary Fig. S6B), essentially as previously reported [25, 54, 110].

Mutants translocated into the nucleus upon cell stimulation with 100 nM Dex (Supplementary Fig. S6A), although GR^{P625A} remained partly cytoplasmic after 40 minutes. Successful nuclear translocation suggests that neither the folding of the receptor nor its interactions with the import machinery were significantly affected. GR^{P625A} was mostly monomeric in the nucleoplasm and could not be detected at the MMTV array (Fig. 3B), consistent with a recent report [111]. A 10-fold higher Dex concentration was barely able to increase the dimerization of this variant, and even at this concentration, no signal was detected at the array (Fig. 3B). To assess whether this behavior could be reverted by enforced tetramerization of the receptor, we also generated and tested the double mutant GR^{P474R/P625A}. Variant GR^{P474R}, also known as GR^{tetra}, forms tetramers both in the nucleoplasm and at the array (Fig. 3A and B) [25]. Although introduction of this exchange in the DBD did not modify the monomeric character of the GR^{P625A} mutant in the nucleoplasm, it did rescue tetramerization when bound to DNA, indicating a complex, intertwined relationship between DBD and LBD domains within the FL-GR. Dimerization of mutant GR^{Y545E} was also impaired

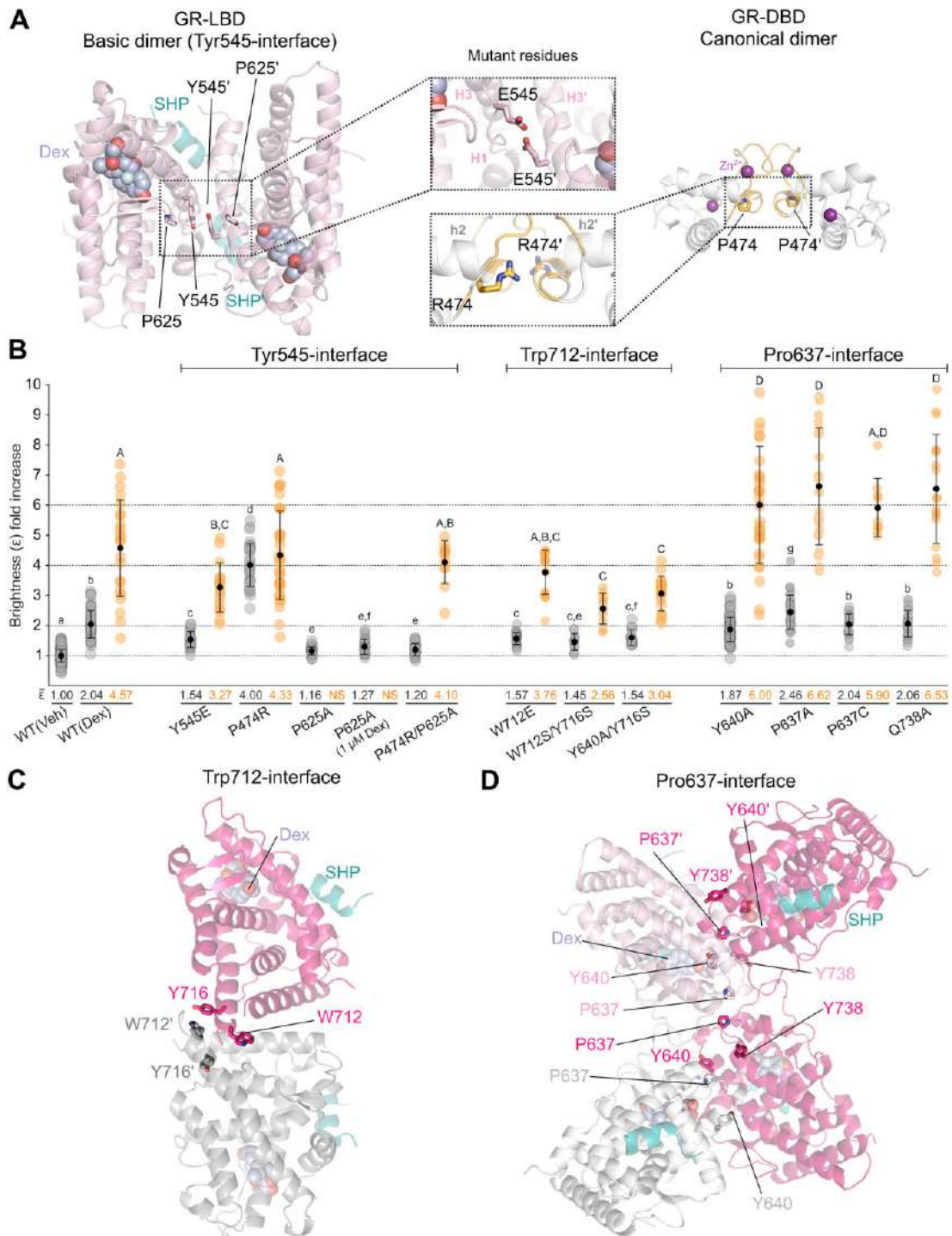


Figure 3. The Tyr545- and Trp712-centered interfaces are crucial for FL-GR self-assembly, while the Pro637 interface promotes multimerization at the DNA array. **(A)** 3D representations of the Tyr545-centered LBD homodimer (to the left) and the canonical DBD homodimer (to the right). The SHP coregulator peptides and Dex molecules bound to the LBD are color-coded as in Fig. 1. Residues mutated in the current investigations are shown as color-coded sticks and labeled. The central panels show close-ups of the models with introduced mutations. Note that the presence of glutamate residues at positions 545/545' would result in strong electrostatic repulsion at the LBD–LBD' interface. On the contrary, the replacement of Pro474 in the DBD by a bulkier arginine would allow for important vdW and electrostatic interactions with the neighboring monomer. **(B)** N&B assay. The fold increase in molecular brightness (ϵ), is given relative to the value for the nonstimulated WT receptor (vehicle, Veh). The results in the nucleoplasm and at the array are represented as gray- and gold-colored dots, respectively. Results for the GR^{P474R} variant were taken from our previous publication [54] and are shown here for comparison purposes only. Note that no signal was observed for the GR^{P625A} mutant at the array (NS). The sample mean is shown as a black point in the middle of each dot plot, together with the standard deviation bars. Dot plots with different superscript letters are significantly different from each other ($P < 0.05$, one-way ANOVA followed by Tukey's multiple comparisons test). Statistical analysis of the nucleoplasm and array data were done separately (small and capital letters, respectively). **(C, D)** 3D representations of major dimer-of-dimers interactions in the current crystal. Trp712-centered dimer [C:M, panel (C)] and the central B/C/E/H tetramer in the Pro637 setting (panel D) are represented. Interface residues mutated in the current investigation are shown as color-coded sticks and labeled according to the numbering of the crystallized ancGR2 construct. The SHP coregulator peptides and Dex molecules are color-coded as in Fig. 1.

in the nucleoplasm, although to a lesser extent ($\epsilon = 1.54$), as well as tetramerization at the array ($\epsilon = 3.27$) (Fig. 3B). These findings demonstrate a large impact of the noncanonical, L1–3-centered interface on receptor dimerization within living cells.

MD simulations reveal the differential impact of point mutations at positions 545 and 625 on receptor dimerization

To investigate the effects of mutating interface residues on the tertiary and quaternary structure of GR-LBD, we conducted four independent 1 μ s MD simulations of monomeric WT human GR-LBD, the single-point mutants, Tyr545Glu, Pro625Ala, and Trp712Glu, and the double mutant, Trp712Ser/Tyr716Ser. All systems rapidly reached equilibrium with fluctuations around 1 Å (Supplementary Fig. S7A), indicating that none of the mutations significantly affect the overall domain structure and stability. In all cases, flexibility was primarily limited to loops L1–3, L6–7, L11–12, and most significantly to L9–10, along with the N-terminal end of H10 (Fig. 4A), in line with the structural findings (Supplementary Fig. S2A). Histograms of C α (Y545)–C α (P625) distances revealed the presence of major and minor conformations of the L1–3 loop in WT GR-LBD, with its most populated distance at 6 and 7.5 Å, respectively (Fig. 4B). Furthermore, the major conformation of WT GR-LBD closely matches the X-ray crystal structure, with the only exception of the highly mobile L9–10 loop (Fig. 4C).

Despite the overall structural similarity, each mutation uniquely influenced the conformation of the noncanonical dimerization interface. These differences are most evident in the histograms of inter-residue distances (Fig. 4B and Supplementary Fig. S7C and D). Notably, the truncation of Pro625 to alanine resulted in a more compact structure, as indicated by decreases of about 1.25 and 0.75 Å in the medians of the major and minor inter-residue distance distribution, respectively. A closer inspection of the major conformation reveals a coordinated approach of L1–3 and L5–6 loops, resulting in the clamping of the Tyr545 side chain through close vdW contacts with the Ala625 methyl group (Fig. 4D). In the less populated conformation, the Tyr545 phenolic ring swings towards the main body of the domain and docks onto the Arg569 side chain (Supplementary Fig. S7E). Therefore, none of the conformations of the L1–3 loop in mutant Pro625Ala are compatible with homodimer formation. Less dramatic rearrangements were observed in the Tyr545Glu mutant, where the Glu545 side chain rotates towards the globular module and forms strong salt bridges with Arg569. This mutant-specific interaction not only preserves the overall path of the L1–3 loop but also stabilizes the Arg569 side chain in a dimerization-compatible conformation (Fig. 4E). In this mutant, however, the distribution of inter-residue distances indicates greater flexibility of the loop compared to both WT and Pro625Ala (Fig. 4B and Supplementary Fig. S7C and D).

Finally, the mutation of aromatic H10 residues Trp712 and Tyr716 triggered both local and distant effects. Unexpectedly, in the case of the single point mutant Trp712Glu, the L9–10 loop becomes more flexible than in the WT domain. In contrast, the double mutation Trp712Ser/Tyr716Ser results in a more flexible N-terminal half of the loop, while the C-terminal part becomes rigidified (Fig. 4A). Notably, these changes in

H10 have a distinct impact on the distal L1–3 loop, which becomes more rigid in both cases, contrasting with the higher flexibility observed in the Tyr545Glu and Pro625Ala mutants. Furthermore, the minor conformation is absent in both H10 mutants. These findings confirm and extend the results of previous MD simulations [101] and align with previous crystallographic evidence [100]. Altogether, the current MD results provide a straightforward explanation for the larger impact of the Pro625Ala mutation on the L1–3-centered dimerization interface. Furthermore, the important role played by Arg569 in this regard explains the deleterious impact of the Arg569Gln mutation in a patient with reversible GC resistance (Supplementary Table S2) [102].

Crosslinking-mass spectrometry reveals dominant L1–3 and H9/L9–10/H10 interfaces in solution, supporting a model of tetrameric FL-GR

The findings presented above strongly suggest that the L1–3 stretch centered on Tyr545, and stabilized by L5–6 residues like Pro625, is essential for GR homodimerization *in vivo*. This, along with some features of the PDB 7PRW structure such as the small area and polar character of the LBD–LBD' interface (Supplementary Fig. S8A–C), prompted us to re-interpret this structure to generate a model of multidomain GR consistent with the current structure (Supplementary Fig. S8D and E and Supplementary Video S3). Briefly, both the DBD–DBD' canonical interface and the interacting DBD–LBD pair (from the 7PRW structure) were left unmodified. This unmodified GR DBD–LBD monomer in cyan at Supplementary Fig. S8A is here referred to as 'monomer A'. Repositioning 'monomer B' (the second LBD' monomer in marine blue) into the parallel Tyr545/Tyr545' conformation (Supplementary Fig. S8D and E) generated a homodimer where the more C-terminal stretch of its L1–3' loop (Tyr548'–Val552') interacts with the topologically equivalent residues contacted by mon A (Arg479' and Gln483') (Supplementary Fig. S8F). In this manner, the Tyr545-dimer satisfies the constraints imposed by the canonical, DNA-bound DBD–DBD' homodimer, while also facilitating important DBD'–LBD' interactions for monomer B (Supplementary Fig. S8G and H). Moreover, this model predicts favorable intermonomer interactions at the DBD'–LBD interface (Supplementary Fig. S8H). In particular, the Arg460' side chain would compensate for the negative electrostatic potential of Glu537 and Glu661, in addition to forming a salt bridge with Asp462 in the DBD. The DBD–LBD/DBD'–LBD' homodimer interface is conceptually reminiscent of the "convergence zone" described by Rastinejad and co-workers [112].

To better characterize GR self-assembly in solution and overcome the limitations of using only the LBD module, we overexpressed and purified a multidomain GR construct (DBD–hinge–LBD tandem). We first confirmed that this recombinant multidomain GR binds a double-stranded DNA fragment containing the GRE of the major GR-target gene, SGK1 (Fig. 5A). In these experiments, we consistently observed two protein–DNA bands, indicating the formation of both dimeric and tetrameric GR–DNA complexes in solution.

Next, we took advantage of the presence of several solvent-exposed lysine residues across all three structural elements of multidomain GR to conduct XL-MS experiments. We used two cleavable crosslinkers, DSSO (10.1 Å spacer arm) and DSBU (12.5 Å spacer arm). The MS/MS data clearly showed

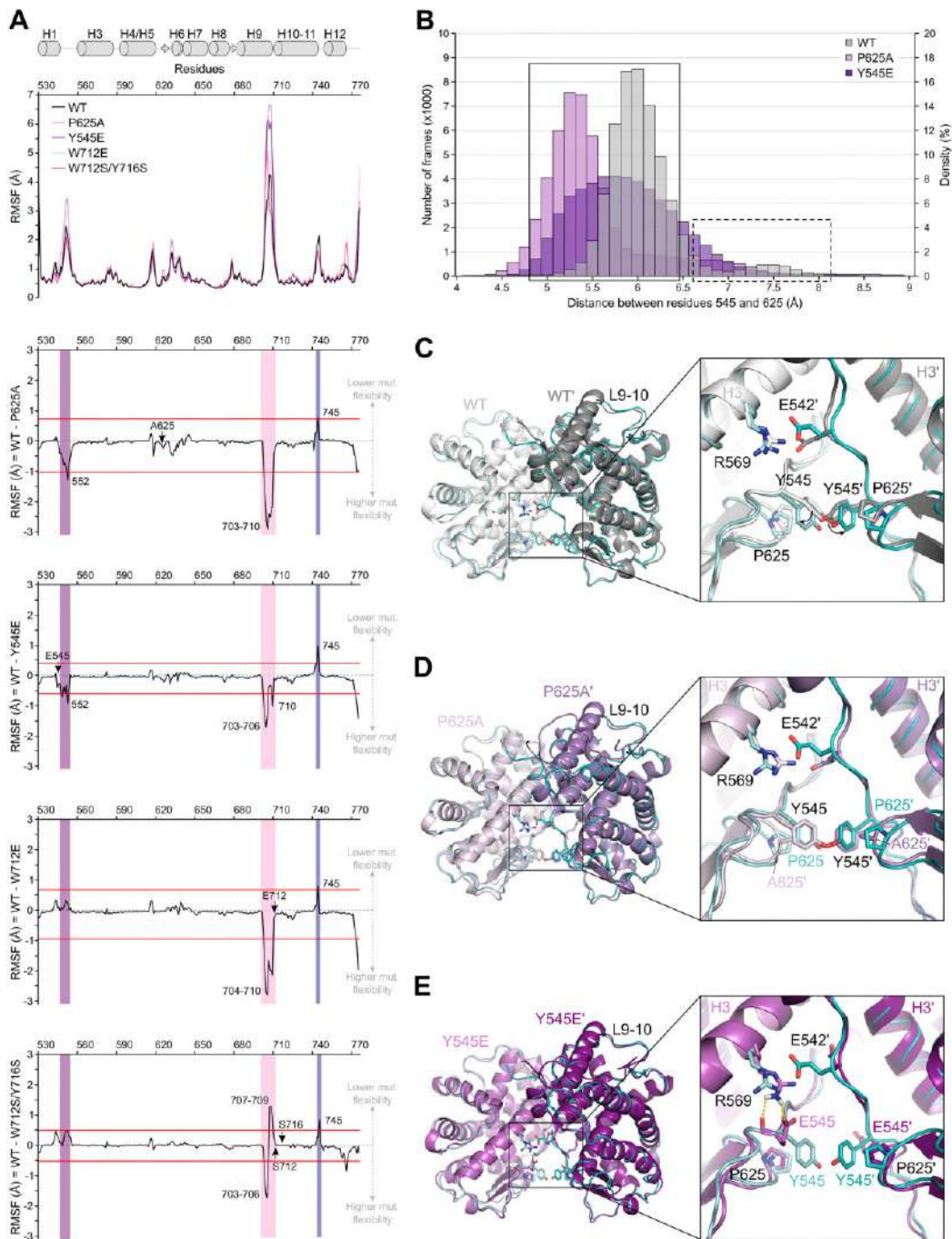


Figure 4. Point mutations of residues Tyr545 and Pro625 differentially affect the noncanonical dimerization interface of GR-LBD. **(A)** The upper panel illustrates the secondary structure of GR-LBD. Below this, we present the RMSFs of WT GR-LBD and the four studied mutants along the domain sequence, color-coded as indicated. Additionally, we also show the RMSF differences between the WT domain and each of the individual mutants. Particularly large differences are highlighted with bars colored according to the affected GR-LBD face (Front in purple, Top in pink and Back in blue). **(B)** Histograms of the distances between C α atoms of residues at positions 545 and 625 in WT GR-LBD and mutants Tyr545Glu and Pro625Ala. The number of frames and their frequencies are plotted as a function of this distance. Results are based on the four independent 1 μ s MD simulations conducted for each studied system. Major and minor populations are marked with solid and dashed boxes, respectively. Note that the distribution is shifted to the left in the Pro625Ala mutant, indicating a more rigid structure. In contrast, the bell-shaped distribution for Tyr545Glu suggests the exploration of a wider range of L1–3 conformations in this case. **(C)** Overall similarity of calculated and experimental structures. The major conformation of WT GR-LBD was superimposed on crystallographic monomers G and H. The close-up to the right shows the L1–3–centered, noncanonical dimer interface. Note that simple rotations of the Glu542/Glu542' and Tyr545/Tyr545' side chains facilitate intermonomer interactions, thereby stabilizing the GR-LBD homodimer, as observed in the crystal structure. **(D)** Comparison between the major conformation of mutant Pro625Ala and the crystallographic G-H dimer. Note in the close-up of the dimer interface that the Tyr545 side chain is stabilized by strong vdW contacts with the Ala625 methyl group, which points towards the center of the phenolic ring. All distances between Ala625 C β atom and the carbon atoms in the phenolic ring of Tyr545 range between 3.5 and 3.9 Å. In the resulting rigidified structure, the Tyr545/Tyr545' side chains are not positioned to stack on each other but would rather clash in a homodimer. **(E)** Comparison of the major conformation of Tyr545Glu and the crystallographic G-H dimer. Note the strong salt bridges between the carboxylate of Glu545 and the guanidinium group of Arg569 in the close-up of the dimer interface. This electrostatic interaction stabilizes Arg569 in a conformation compatible with homodimer formation upon rotation of the Glu542' side chain.

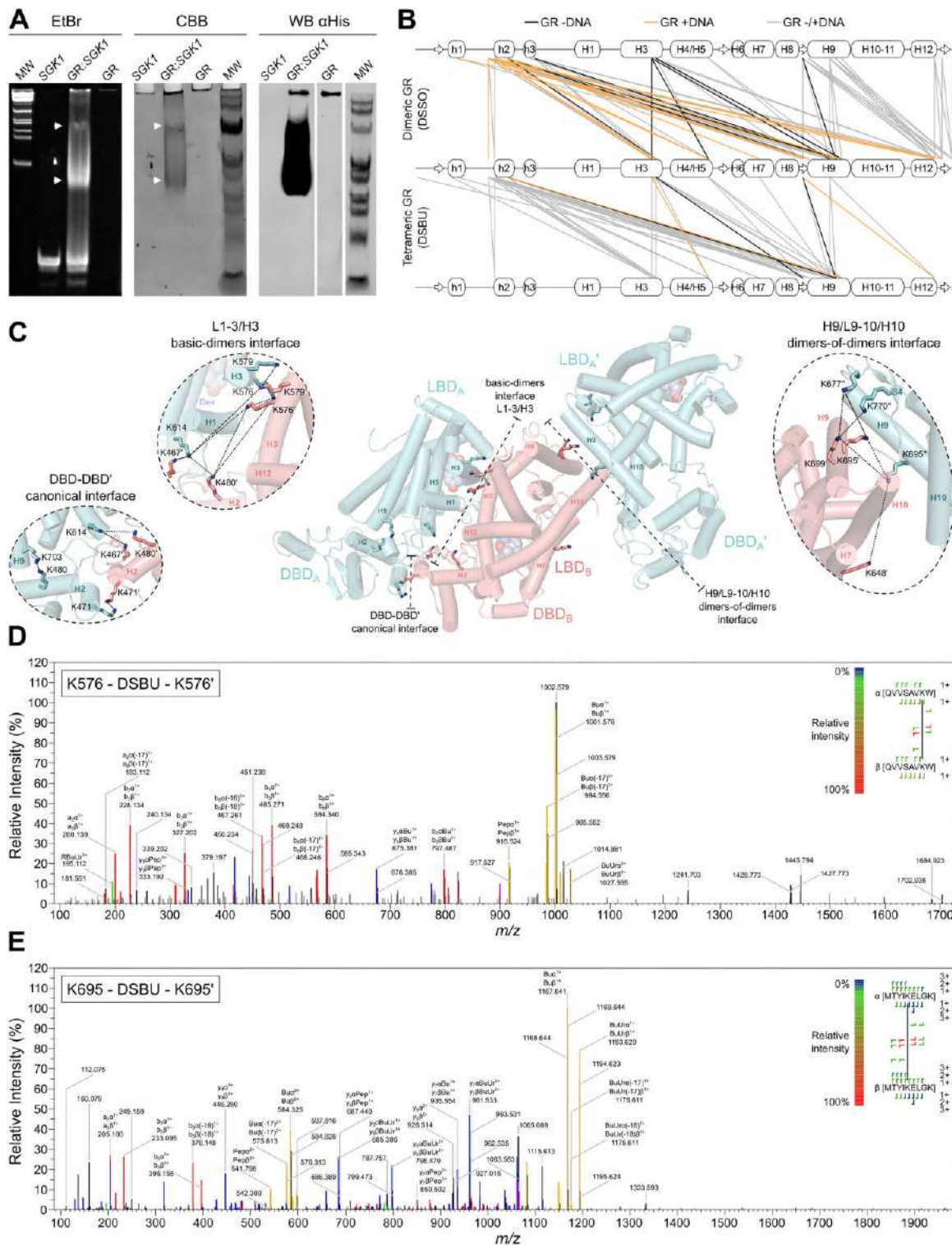


Figure 5. L1-3/H3 and H9/L9-10/H10 regions drive multidomain GR self-assembly in solution, independently of DNA. **(A)** Multidomain GR binds a double-stranded DNA fragment comprising the *SGK1* GRE. The results of a representative experiment are shown. Polyacrylamide gels were first stained with EtBr and visualized under UV light, then stained with CBB. Gels run in parallel were transferred to nitrocellulose membranes and probed with an anti-His antibody (WB; note that the lane for free GR is from a different membrane). **(B)** Summary of four independent XLMS experiments with multidomain GR using cleavable crosslinkers (DSSO for the GR dimer or DSBU for the tetramer). Crosslinks are colored based on their DNA dependency: black indicates those identified only in the absence of DNA, gold for those detected only in its presence, and gray for those found irrespective of DNA presence. Secondary structure elements are indicated; those corresponding to the DBD are designated with lowercase letters. **(C)** XLMS experiments corroborate the involvement of noncanonical L1-3/H3 and H9/L9-10/H10 surfaces in GR self-assembly. The central panel displays a crystallographic dimer-of-dimers; for clarity, only the interacting monomer from the second dimer is shown. Close-ups on the left highlight crosslinked lysine residues at the canonical DBD-DBD' and L1-3/H3 interfaces verified by MS. Those on the right highlight interactions detected between lysines of the H9/L9-10/H10 region and the F-domain (the dimer-of-dimers interface). **(D)** MS/MS spectra demonstrating DSBU-mediated crosslinking between Lys576 residues from two monomers. **(E)** MS/MS spectra demonstrating DSBU-mediated crosslinking between Lys695 residues from two monomers.

the formation of several intermolecular DSSO- or DSBU-crosslinked peptides (Fig. 5B and [Supplementary Table S5](#)). As expected, we detected peptides demonstrating the formation of the canonical DBD homodimer in both DSSO and DSBU experiments, most notably Lys471-Lys471' crosslinked peptides. Importantly, we also identified several peptides bridging lysine residues at positions 576, 579, and 695 from two neighboring monomers (Fig. 5C–E, [Supplementary Fig. S9A–C](#), and [Supplementary Table S5](#)). These findings, along with several additional crosslinks (XLs), provide unambiguous proof for the preferential assembly of GR monomers through the L1–3 and H9/L9–10/H10 regions in solution, consistent with the current crystal structure. Furthermore, our XL-MS results support a mechanism of tetramerization where two L1–3-centered, noncanonical GR homodimers associate through contacts between their H9/L9–10/H10 regions. We observed significant differences in DSSO- and DSBU-crosslinked peptides, most notably the disappearance of XLs between Lys695 and Lys770' in the F-domain. This suggests that more open dimer-of-dimers conformations such as G:K are favored in solution.

The alternative L6–7-centered octameric arrangement of GR-LBD modules ([Supplementary Fig. S4](#)) features more apolar surfaces and lacks in particular suitably positioned lysine residues for DSSO or DSBU crosslinking. Therefore, we cannot confirm the presence of such arrangements in solution. However, XLs between lysine residues at positions 677/677', and especially between the C-terminal lysines at positions 765/765', 770/770', and 777/777', are compatible with another back-to-back arrangement of multidomain GR monomers. This arrangement closely resembles homodimer #17 from our catalog ([Supplementary Table S5](#) and [Supplementary Fig. S9D](#)), which derives from the structure of cortisol-bound GR-LBD (PDB entry 4P6X) [106]. Furthermore, we observed several nonsymmetrical XLs also consistent with this arrangement ([Supplementary Table S5](#)). Assigning these crosslinks is more problematic, and they could, at least partly, correspond to intramolecular XLs. Nevertheless, the intriguing observation that they were found exclusively in dimers of multidomain GR, not in tetramers, supports the presence of this back-to-back conformation in solution, which is incompatible with the more stable Trp712-centered dimers-of-dimers.

Other arrangements, inferred from the XL-MS results, suggest that either the L1–3 loop or the H9/L9–10/H10 region can be found close to the canonical inter-DBD interface ([Supplementary Table S5](#)). We believe that these XLs correspond to transient, likely inactive receptor conformations, as they would impair homotypic interactions of the DBD and/or LBD modules. Finally, we detected several crosslinks between Lys498 in the interdomain connector and LBD lysine residues at major intermonomer interaction sites (e.g. Lys576 and Lys579 in L1–3; Lys695 and Lys699 in H9; Lys765 and Lys770 in the F-domain). Additionally, XLs were detected between Lys495/Lys496 and Lys695' in H9. The absence of crosslinks involving other lysine residues in the DBD–LBD linker suggests that this long peptide is highly flexible in solution, even when the receptor is DNA-bound, and does not adopt a single fixed conformation. We did not detect hinge XLs in the DSBU experiments, which is consistent with the involvement of L1–3 and H9/L9–10/H10 regions in intermonomer contacts.

Although multidomain GR formed both dimers and tetramers irrespective of whether GRE-containing oligonucleotides were present, DNA binding significantly impacted multimerization. Most notably, DNA promoted the stabilization of both the Y545-centered and DBD–LBD interfaces, a conclusion supported by the increased number and confidence of identified crosslinked peptides ([Supplementary Table S5](#)). These findings align with the established role of DNA as an allosteric GR modulator [113].

The Trp712 interface is important for receptor tetramerization on chromatin and transcriptional activity

Having established the central role of Tyr545-centered, non-canonical homodimers in living cells, we next explored the possible relevance of observed dimer-dimer interactions for receptor multimerization. The identification of several Trp712-centered dimers-of-dimers in the current structure, the realization that these contacts are common in previously reported structures and are also populated in solution [54], and the fact that residues such as tryptophans and tyrosines are enriched in bona fide PPI surfaces [103–105] prompted us to assess the possible impact of this arrangement in living cells. Firstly, we performed docking experiments to generate 12 000 different dimers-of-dimers using a state-of-the-art protein-protein docking procedure without imposing any constraints (see [Supplementary Fig. S10A](#) and the 'Materials and methods' section). These solutions were ranked according to their pseudo-energy values, as previously described [54, 80]. The results of these experiments revealed that the Pro637- and Trp712-centered areas are hotspots for homotypic interactions, as indicated by their high NIP values ([Supplementary Fig. S10B](#) and C). Overall, we found 296 and 422 docking solutions that closely match the symmetric arrangements centered on Pro637 and Trp712 (respectively) observed in the current crystal, among them one of the top 20 solutions each ([Supplementary Fig. S10D](#) and E). Of note, many of the docking solutions are compatible with the experimentally observed dimers-of-dimers.

Next, we generated both single (GR^{W712E}) and double mutants (GR^{W712S/Y716S}) of the most exposed aromatic residues at the interface ([Supplementary Fig. S6A](#)). We also generated and tested a variant that truncates the two aromatic residues at the alternative LBD–LBD' interface, GR^{Y640A/Y716S}. Similar to the mutants of the Tyr545 interface described above, these variants were correctly expressed and trafficked to the nucleus upon Dex treatment ([Supplementary Fig. S6B](#)). Unexpectedly, all mutants showed reduced receptor dimerization in the nucleoplasm (ϵ values ~ 1.5 , Fig. 3B and C), suggesting an impact on noncanonical, Tyr545-mediated homodimer formation either because of impaired DBD–LBD contacts and/or through allosteric modification of the L1–3 loop (see above). Mutant GR^{W712E} formed tetramers at the array ($\epsilon = 3.76$), while simultaneous replacement of the aromatic Trp712 and Tyr716 residues by the less bulky serine resulted in severely impaired tetramerization ($\epsilon = 2.56$) (Fig. 3B), demonstrating a role of this interface in tetramer formation within the context of the FL-GR. Finally, the GR^{Y640A/Y716S} mutant showed an intermediate behavior ($\epsilon = 3.0$), thus reverting the tendency to the formation of higher-order oligomers of the GR^{Y640A} variant (compare Fig. 3B and D).

Formation of Tyr545-centered basic dimers and Trp712-centered dimer-of-dimers is essential for GR transcriptional activity

To verify whether disruption of the noncanonical dimerization interface also affects the biological activity of the receptor, we performed RNA-seq analyses of cells stably expressing variant GR^{P625A}. The results of these transcriptomic analyses revealed an almost complete loss of transcriptional activity of the GR^{P625A} mutant (Fig. 6A and B). Furthermore, the nine hypersensitive genes activated by GR^{P625A} showed significantly lower levels of stimulation than the WT receptor (Fig. 6A and B). Altogether, these results indicate that the parallel, Y545-centered GR homodimer is the major active conformation in living cells, and that receptor dimerization is essential for DNA binding and transcription. Because a recently presented structure of multidomain GR features an LBD dimer in which residues of the L6–7 loop and H7 dock onto the N-terminal end of helix H10 (PDB 7PRW) [55], we also generated and studied by N&B the GR^{Y640A} variant. This mutant remained essentially dimeric in the nucleoplasm. Unexpectedly, truncation of the Tyr640 side chain to alanine promoted the formation of higher-order oligomers on DNA ($\epsilon = 6.0$, indicative of either hexamers or mixtures of higher and lower oligomers; see also below) (Fig. 3B). We had previously reported a similar behavior for the Chrousos syndrome mutation, GR^{D641V} [54].

Unexpectedly, the GR^{W712E} variant exhibited an almost complete lack of transcriptional activity (Fig. 6C and D), activating only about 10% of the genes compared to the WT receptor. On the other hand, the GR^{W712S/Y716S} double mutant was also transcriptionally impaired, although to a lesser extent (Fig. 6C and D, ~60% of the genes). These results illustrate the complexity of the GR structure-function relationship and suggest that the dimers-of-dimers centered on the Trp712/Phe715/Tyr716 aromatic triplet play an important role in receptor tetramerization, resulting in gene transcription tempering in living cells.

Allosteric pathways linking L1–3, L6–7, and L9–10 loops

We recently demonstrated that the p.Asp641Val mutation, associated with Chrousos syndrome, enhances FL-GR multimerization in living cells upon DNA binding [54]. Specifically, the GR^{D641V} variant formed higher oligomeric structures at the array in N&B assays ($\epsilon = 7.19$), suggesting a complex mixture of stoichiometries including tetra-, hexa-, and octamers. Precisely, octamers formed in the current crystals feature one GR-LBD molecule with an Asp641 carboxylate that docks into an aliphatic pocket formed by the side chains Leu636'/Pro637' from a neighboring monomer (Supplementary Fig. S4B). A valine side chain would engage in more favorable vdW interactions with the apolar Leu636/Pro637 side chains, which provides a straightforward explanation for the increased tendency to form higher-order oligomers by the GR^{D641V} variant. A similar multimerization behavior in living cells was observed for the previously studied variant, GR^{P637A} ($\epsilon = 6.62$) [54], as well as for two mutants of the Back LBD face generated in the current investigation, GR^{P637C} and GR^{Y640A} (Fig. 3B and D). Therefore, we decided to assess whether other mutations of nearby residues at the Back surface also generated higher-order multimers at the array in live cells. Indeed, this was the case for the alanine variant of a more distant

residue, Gln738 ($\epsilon = 6.53$; Fig. 3B and D). These N&B results confirmed that the mutation of residues at the Pro637 interface does not affect GR dimerization, but invariably promotes the formation of higher-order oligomers at the array. Furthermore, transcriptomic analysis of the GR^{P637A} mutant indicated a two-fold reduction in the number of activated genes (Fig. 6E and F), similar to our previous results with the Chrousos variant, GR^{D641V} [54].

To explore the possible relevance of other known NR3C1 point mutations and single nucleotide polymorphism (SNPs) for the structure and function of the GR, we mapped all GR-LBD variants reported to date on the 3D structure of the domain (Fig. 7A; major clinical and structure-function information on these variants is summarized in Supplementary Table S2). Noteworthy, several SNPs in addition to Asp641 replace a polar or charged residue by one with an aliphatic or aromatic side chain, not only in L6–7/H7 (e.g. p.His645Tyr) but also in the nearby L11–12 loop (p.Asp742Val, p.Lys743Met, p.Ser746Ile) or the F-domain (p.Ser765Leu). Intriguingly, some of these mutants would stabilize the back-to-back conformation identified in our XL-MS experiments (Supplementary Fig. S9D and Supplementary Table S5). This is in addition to another similar mutation linked to PGGR, p.Thr556Ile (Fig. 7A) [39, 114]. These variants are likely to enhance receptor multimerization, similar to GR^{D641V}. Other missense variants cluster in and around well-characterized functional sites, the LBP (p.Met560Arg, p.Ala605Thr), and the AF-2 cleft (e.g. p.Val575Gly, p.Gln597Pro/His/Glu, p.Glu755Val), but also at the dimerization (e.g. p.Ser551Tyr, p.Ile559Asn), and tetramerization interfaces (SNPs affecting positions 689, 697, 699–701, and 703 in H9, 708–711 in L9–10/N-terminus of H10, and mutants p.Arg714Gln/Leu/Trp in this helix) (Fig. 7A). Furthermore, paths cross-connecting the two flexible poles of the module are enriched in disease-linked residues: from L9–10/H10 (Arg714) to the L1–3 loop (Tyr545) and H3 (Arg569) through L7–8 and H5 (the 'lower path' in the left panel of Fig. 7A), or through H9/H10 and the LBP (the upper path). This is in line with functional studies indicating reduced affinity for Dex and impaired interactions with coregulators for several mutations of residues distant from both LBP and AF-2 (Supplementary Table S2) [37, 40, 115–119]. These circuits cross-connecting the major functional areas of GR-LBD are evolutionarily conserved from fish to humans.

Discussion

We integrated biophysical techniques (X-ray crystallography and XL-MS), MD simulations, and *in cellulo* analysis of point mutants (using fluorescence microscopy and RNA-seq) to elucidate the multimerization mechanism of the GC receptor. This orthogonal approach refined our catalog of multimeric GR arrangements and illuminated their functional relevance *in vivo*. Specifically, we present compelling evidence that the L1–3 loop, particularly the Tyr545 side chain, is critical for receptor homodimerization and subsequent transcriptional activity in living cells. This side chain is optimally positioned for interaction between neighboring GR molecules by residues of the underlying H5–H6 linkers (e.g. Pro625 and Ile628). Our current findings strongly indicate that the parallel orientation of GR-LBD modules predominates *in vivo*, and any perturbation of the Ile628/Pro625/Tyr545 cluster appears to cause a domino-like effect on the noncanonical, Tyr545-centered

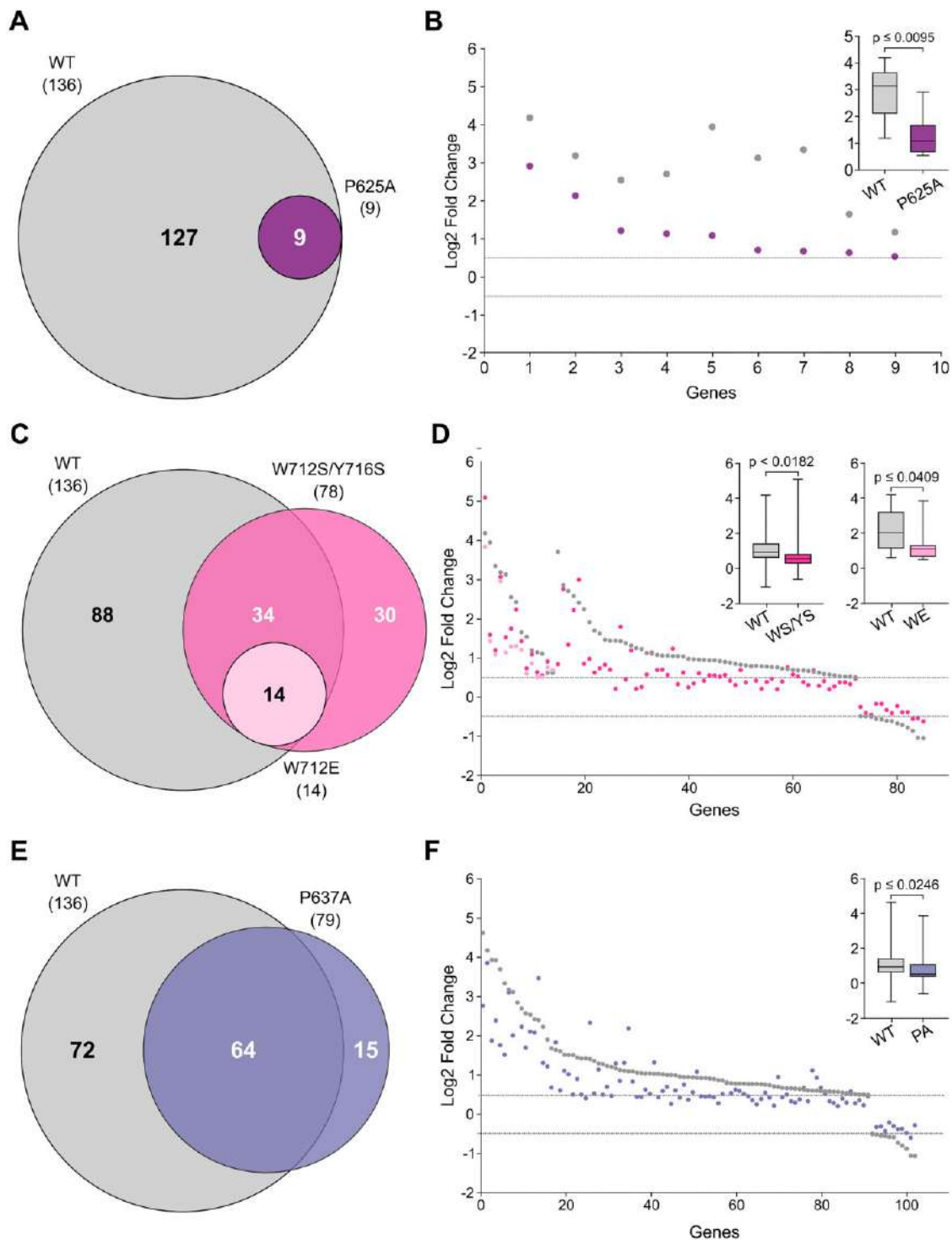


Figure 6. Mutations at Tyr545-, Trp712-, and Pro637-interfaces differently affect GR transcriptional activity. Transcriptomic analysis of the impact of mutations affecting Tyr545- (**A, B**), Trp712- (**C, D**), or Pro637-interfaces (**E, F**). Stable cell lines expressing GFP-tagged mouse FL-GR or shown variants were treated with 100 nM Dex for 2 h for RNA-seq analyses. Three replicates were used per condition. Protein-coding genes were considered to be regulated by the GC if they showed an absolute \log_2 FC > 0.5 at a FDR < 0.01. The *P*-values reported in the comparative analysis were generated using a two-tailed, paired, nonparametric Wilcoxon signed-rank test, performed in GraphPad Prism version 10.1.1. The total number of Dex-responsive genes is given in parentheses in Venn diagrams (**A, C, E**). Dashed horizontal lines in scatter plots (**B, D, F**) denote \log_2 FC \pm 0.5. Box and whiskers plot of the same data displays interquartile range depicting the 25th, 50th, and 75th percentile as box with the median as black bar. (**A, B**) Venn diagram and scatter plot comparing genes regulated upon Dex treatment by variant GR^{P625A}, as compared to the WT receptor. Note that even the nine genes that were up-regulated by GR^{P625A} were transcribed at significantly lower levels. (**C, D**) Venn diagram and scatter plot comparing genes regulated upon Dex treatment by variants GR^{W712E} and GR^{W712S/Y716S}, as compared to the WT receptor. Note the severely impaired transcriptional activity of variant GR^{W712E}, pointing to an important impact of electrostatic repulsion between Glu712/Glu712' residues at the dimer-of-dimers interface and/or enhanced p23-mediated disassembly of transcription complexes. Less dramatic but also important effects were observed with the double mutant, GR^{W712S/Y716S}. (**E, F**) Venn diagram and scatter plot comparing genes regulated upon Dex treatment by variant GR^{P637A}, as compared to the WT receptor. The scatter plot of shared Dex-regulated genes shows the overall lower transcriptional activity of this mutant.

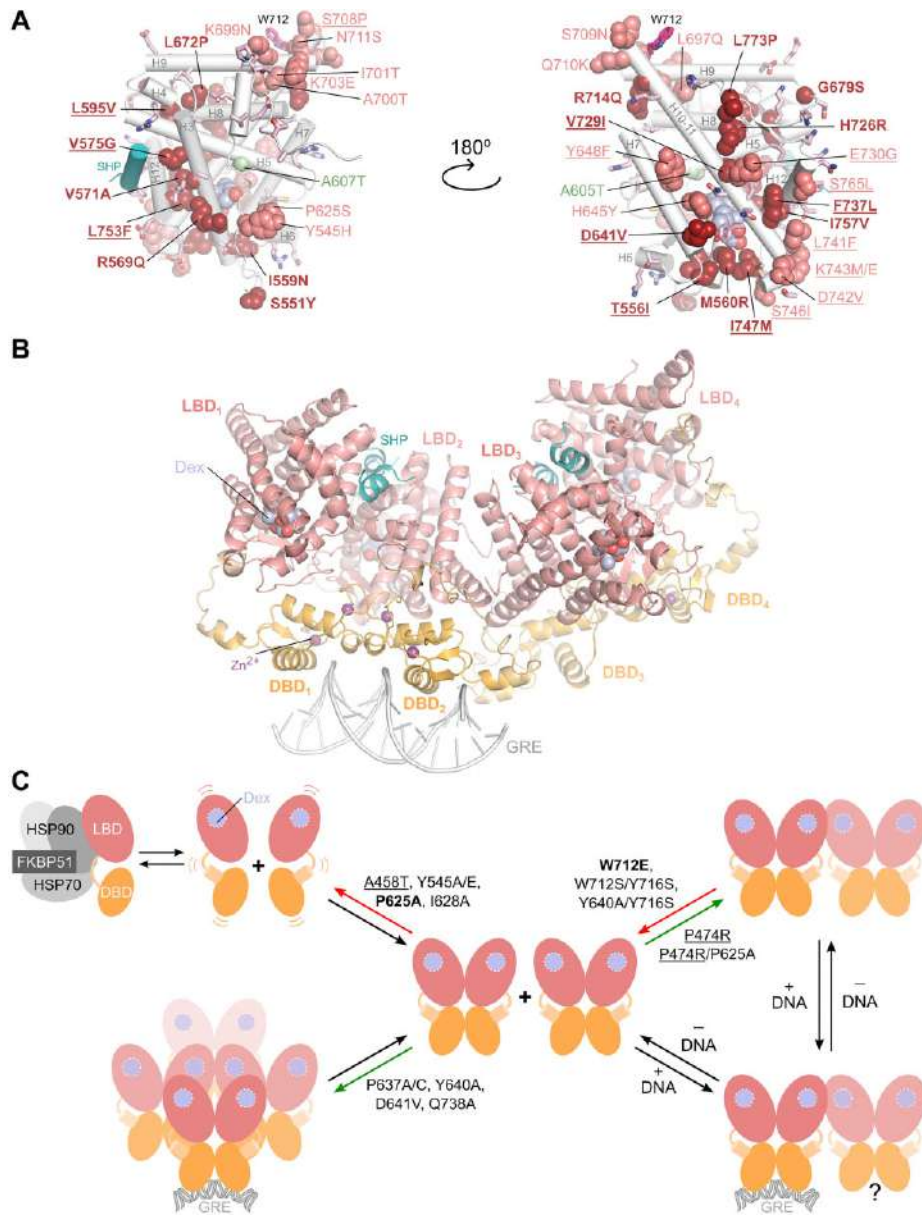


Figure 7. Molecular basis of Chrousos syndrome and suggested pathway of GR multimerization. **(A)** Distribution of missense mutations and SNPs in human GR-LBD. Front and Back faces of the domain are shown in the left and right panels, respectively, with the side chains of affected residues represented as spheres and labeled. Residues have been colored firebrick red to highlight variants identified in patients with Chrousos syndrome, salmon for SNPs that have not been characterized to date but are likely to have an impact on the protein structure and function (e.g. p.Tyr545His, p.Pro625Ser, which are predicted to impair dimerization), and light pink sticks for those SNPs that represent more conservative replacements and are therefore less likely to be deleterious. Variant p.Ala605Thr (green sphere) might increase affinity for GCs, similar to the p.Ala605Val variant in human [100] and porcine GR [134, 135]. Note the clustering of mutations in the functionally relevant L1–3/H3 and H9/L9–10/H10 areas. Note also that several SNPs enhance the hydrophobic nature of the Back face (underlined), similar to the previously characterized GR^{D641V} variant [54], and are therefore likely to result in similar oligomerization behavior. **(B)** Model of tetrameric multidomain GR bound to DNA. All six Trp712-interfaces are compatible with the formation of dimers-of-dimers similar to the one shown in this panel, which corresponds to the A-B:O-P arrangement. Note that tetramerization essentially depends upon LBD-mediated interactions but does not involve contacts between DBD dimers. **(C)** Proposed pathway leading to GR multimerization and activation of transcription. GR folding requires the coordinated actions of chaperones Hsp70 and 90, cochaperone p23 and immunophilins. Two approaching monomers can dimerize by sequential DBD–DBD' (through residues of the second zinc finger) and LBD–LBD' interactions (through the Tyr545 surface). Dimerization stabilizes intra-monomer DBD–LBD and DBD'–LBD' contacts mediated by residues of the L1–3 or L9–10 loops, respectively, along with additional intermolecular interactions. GR dimers, rather than monomers, can then independently 'scan' the chromatin landscape [73], followed by the recruitment of coregulators, which ultimately activates transcription. DNA binding triggers a conformational change, leading to tetramerization through contacts between the Trp712-centered surfaces, which might enhance the transcriptional output. Based on our results, the impact of point mutations on the oligomeric state of the receptor is indicated (DBD mutations are underlined). Mutations that have the highest effect on GR transcriptional activity are in bold. For simplicity, association events are presented sequentially, but are likely highly coupled *in vivo*, and therefore most mutations have pleiotropic effects on the multimerization process. Most notably, mutations at the H9/L9–10/H10 zone affect monomer conformation (through impaired contacts with the DBD), dimerization (via allosteric effects transmitted to L1–3), and tetramerization (by impairing dimer-of-dimers formation). Finally, the kinetics of the multimerization process is influenced not only by the concentrations of GR and GCs, but also by the presence of specific coregulators and the chromatin state (not illustrated in the figure for simplicity). See Supplementary Fig. S11 for a thorough classification of studied mutants according to their impact on GR oligomerization.

dimer interface (Figs 3 and 4, and [Supplementary Video S3](#)). This explains the relatively minor impact of the Ile628Ala mutant in previous N&B experiments [25], contrasting sharply with the significant effect of the central Pro625 residue demonstrated in our study (Figs 3 and 4) and by others [4, 111].

While other topologically distinct arrangements of GR-LBD modules could accommodate the canonical DBD homodimer by stacking two Tyr545 side chains ([Supplementary Fig. S1](#)), they would result in much weaker DBD'-LBD' contacts. Nevertheless, these conformations might still play a role during initial receptor dimerization. Our results also reveal strong structural and thermodynamic coupling, not only between the DBD-DBD' and LBD-LBD' protein-protein dimerization interfaces, but also with protein-DNA interactions. For example, the double mutant GR^{P474/P625A} remained monomeric in the nucleoplasm but formed tetramers when bound to the MMTV array. This aligns with the observation that GR-DBD monomers adopt different relative orientations in free and DNA-bound homodimers [50–52].

Furthermore, the interdimer contacts observed in our current structure appear crucial for receptor multimerization. Our N&B results indicate that the second most populated interface in the crystals, formed by residues of the H9/L9–10/H10 area, plays a critical role in FL-GR tetramerization. This finding is strongly supported by our XL-MS studies, which identified top-to-top dimers that cross-connect residues of H9, L9–10, and the F-domain as a major hotspot for intermonomer interactions (Fig. 5C). Our findings also indicate that the three nearby, exposed aromatic residues at the N-terminus of H10 –Trp712, Phe715, and Tyr716– are a key element of the dimer-of-dimers interface. However, likely owing to the significant flexibility of this interface, point mutations of these aromatic residues had important differences on receptor self-assembly in living cells. Specifically, the previously characterized GR^{W712A} mutant showed only a minor impact on receptor multimerization [54]. In stark contrast, the GR^{W712E} variant profoundly affects multimerization and, critically, transcriptional activity. Despite normal nuclear trafficking, GR^{W712E} activates only the same limited set of hypersensitive genes as GR^{P625A}. This unexpected finding points to a more significant role for electrostatic repulsion at this interface, possibly reducing the nuclear dwell time of the GR^{W712E} variant. Additionally, the Glu712 carboxylate could form strong, solvent-protected salt bridges with Arg122 in the cochaperone p23 [17]. This interaction would lead to more efficient disassembly and delayed re-assembly of transcription complexes organized around GR^{W712E} [113]. The finding of a more compact, closed conformation, characterized by an enlarged helix H10 in these dimers-of-dimers, supports the broader trend of enhanced secondary structure formation at the expense of irregular regions or loops at PPI interfaces [104, 105]. We also note that H9 contains the only characterized PTM of the GR-LBD: the SUMOylation of Lys703 [120, 121], which increases GR transcriptional activity [121].

The Trp712/Phe715/Tyr716 aromatic triplet engages in important interactions with loops L1–3/L6–7, helices H9/H11, and/or the C-terminal F-domain in several previously reported crystal structures (homodimers 7, 8, 13, and 18–20 in our catalog [54]). Additionally, other symmetric arrangements of GR-LBD modules feature two topologically distinct, ‘collapsed’ SF-3 cavities [10]—closely packed triplets of aromatic residues—as seen in PDB entry 5UC3 (a domi-

nant negative mutant of GR α , GR^{L733K/N734P}, complexed with mifepristone), and in 6NWK/6NWL (ancGR2-LBD bound to either Dex or hydrocortisone) [122]. These diverse arrangements reflect the intrinsic tendency of solvent-exposed aromatic residues, particularly those at the N-terminus of H10, to engage in PPIs. While these arrangements are less relevant for GR function *in vivo*, we cannot completely rule out their role in certain pathophysiological settings. It is worth noting that the Trp712-centered interface has been postulated by others as the major GR dimerization interface [123]. However, our current results suggest that this protein surface is critical for receptor tetramerization instead. While N&B data indicate an indirect effect in receptor dimerization, this is likely mediated by allosteric pathways connecting the L1–3 and L9–10 loops. This aligns with our previous N&B findings, which showed dimerization of the (A458T, I628A) double mutant (GR^{mon}) at the array [25].

A third pathophysiological relevant arrangement, emerging from our current work and previous research, centers on residues within the L6–7 loop and the N-terminus of H7, along with nearby residues in L1–3 and H11/L11–12. Notably, alanine truncation of Pro637 (L6–7), Tyr640 (H7), or Gln738 (H11), or replacing the charged Asp641 with an aliphatic valine, consistently led to enhanced receptor multimerization at the array in living cells, with FL-GR forming mixtures of tetra-, hexa-, and octamers (Fig. 3). It is important to note that, in addition to p.Asp641Val, various PGGR-linked mutants, and SNPs are predicted to enhance the apolar character of the GR-LBD's Back surface (Fig. 7A). We highlight that the protected surface areas at these L6–7-centered interfaces are considerably larger than those at the Trp712 interfaces. Indeed, previous studies on Cys638 have already demonstrated an involvement of the L6–7 loop in GC binding and transcription [25, 110]. Because the L6–7 loop is an integral element of the hormone entrance channel to the LBP [124, 125], the observed impact of these mutants on GC binding compounds the deleterious formation of nonproductive multimers. Exchanges that increase the hydrophobic character of this surface would effectively trap the receptor in higher-order multimers. However, considering the exacerbated multimerization propensity of mutants affecting the Back GR-LBD face, we cannot exclude the possibility that these L6–7-centered complexes are relevant for condensate formation, a process known to modulate coactivator recruitment [31, 126]. Alternatively, distinct sets of dimers, trimers, and tetramers of dimers, utilizing different L6–7 arrangements, could function independently in long-range chromatin interactions and chromatin opening [127–130].

Other oxosteroid receptors are known or predicted to rely on topologically equivalent elements for multimerization. For instance, two peripheral AR monomers dock onto the BF-3 regions of the active AR homodimer through their L6–7 loops. This interaction involves key aromatic residues: Tyr632, His635, and Tyr640 (numbered according to the equivalent human GR residues) [14, 131]. The resulting tetrameric arrangements might explain our previous observation of FL-AR multimers both in the nucleoplasm and at the array [25]. On the other hand, although the Trp712/Phe715/Tyr716 aromatic triplet is strictly conserved in GR's closest relative, the MR, nearby nonconservative replacements—especially the Gly698Arg exchange—promote a fundamentally different, antiparallel arrangement of MR-LBD modules. In this configuration, the Trp712 side chain docks onto the guanidinium

group of Arg698, as evidenced in several crystal structures of MR-LBD. It is conceivable that these specificities of the H9/L9–10/H10 surface play a major role in receptor multimerization [27, 72], and could also underlie the formation of distinct GR–MR heterodimers [132]. Taken together, this interface emerges as a major regulator of multimerization across oxosteroid receptors. Given the near identity of all steroid receptors DBDs and the overall conservation of residues shaping their hormone binding pockets, the unique transcription programs activated by these NRs may largely depend on the formation of distinct multimeric arrangements on chromatin.

In summary, current structure and function information can be integrated into the following proposed pathway for GR multimerization and transcription activation (Fig. 7B and C, and [Supplementary Fig. S11](#)). GR is initially maintained in a monomeric, partially unfolded state by interactions with the Hsp90-p23 ‘maturation complex’, within which the Ser519–550 stretch (comprising the hinge, H1, and L1–3) adopts a fully extended conformation [17]. Upon nuclear import and eventual receptor dissociation from the chaperone complex, this N-terminal peptide completes the folding of the GR-LBD module. Several simultaneous interactions then prime the newly folded GR molecule for dimerization-competent conformations. These include intra-LBD allosteric pathways connecting the L1–3 and L9–10 loops, and intra-monomer interactions of these loops with the DBD domains. Dimer formation involves synergistic DBD–DBD’ and LBD–LBD’ interactions mediated mainly by the C-terminal zinc-finger modules and the L1–3 loops, respectively. Once formed, these Tyr545-centered homodimers can independently ‘sample’ the chromatin landscape [30, 34, 35]. Current evidence indicates that interaction with a single GRE suffices to trigger transcription [20]. However, the binding of two GR dimers to appropriately oriented, spatially proximal DNA sequences offers an additional advantage. This arrangement allows contacts between their H9/L9–10/H10 surfaces, forming more stable, transient tetrameric complexes on chromatin that effectively organize the transcription machinery. Furthermore, such complexes might increase the local concentration of active dimers near chromatin, thereby facilitating the efficient transfer of the transcriptional machinery to adjacent transcription start sites. The essential role of DNA in this process is highlighted by our previous finding that DNA binding triggers GR tetramerization in living cells [25, 26], along with its established role as an allosteric modulator of GR structure [20].

Our current model suggests that receptor multimerization is not a hierarchical process, but rather the result of concerted, multidirectional intra- and interdomain, as well as intermonomer interactions, which are modulated by contacts of the receptor with coregulators and target DNA sequences. These interactions are finely modulated by the receptor’s contacts with coregulators and target DNA sequences. This explains the profound impact of mutations at the DBD dimerization interface (P474R, GR^{tetra}) on receptor tetramerization, while on the other hand exchanges at the tetramerization site (W712E and W712S/Y716S) significantly influence homodimer formation. Future investigations should establish whether the various dimer-of-dimers assemblies centered on the Trp712 interface correspond to specific DNA sequences, chromatin structures, or coregulators, and if they activate unique transcription programs. Alternatively, these assemblies might represent intermediates in a pathway that involves rear-

rangements of both DNA and transcription factors, ultimately converging in a single, stable transcription complex [133].

Acknowledgements

We thank Erick Ortlund (Emory University) for providing the ancGR2-LBD expression plasmid. We thank ALBA-Cells synchrotron XALOC team for beamline support. MS/MS was performed at the IRB Barcelona Mass Spectrometry and Proteomics Core Facility and we are grateful to Marina Gay and Gianluca Arauz-Garofalo for help with data handling.

This research was supported in part by the Intramural Research Program of the National Institutes of Health (NIH). The contributions of the NIH author(s) were made as part of their official duties as NIH federal employees, are in compliance with agency policy requirements, and are considered Works of the United States Government. However, the findings and conclusions presented in this paper are those of the authors and do not necessarily reflect the views of the NIH or the U.S. Department of Health and Human Services.

Author contributions: G.L.H., P.F.-P., and E.E.-P. designed, supervised the project, and share overall responsibility. P.F.-P. drafted the article. G.L.H. and E.E.-P. obtained financial support. A.A.-M., I.M.-N., and M.A. produced recombinant proteins, performed crystallization trials, and created figures and supplemental videos. A.A.-M., A.J.-P., I.M.-N., M.D., M.V., and P.F.-P. performed and interpreted XL-MS. A.A.-M. and E.E.-P. collected X-ray diffraction data. P.F.-P. interpreted X-ray diffraction data, solved, and refined the structure. P.P. contributed tools and information on human NR3C1 point mutations and SNPs. A.J.-P. and J.F.-R. performed and interpreted docking experiments. M.N.P.-M., P.M.-V., J.P.-P., and J.R.-M. performed and interpreted MDs. A.A.-M., A.J.-P., and T.A.J. generated FL-GR mutants. A.A.-M., A.J.-P., A.L.L., T.A.J., and D.M.P. performed and analyzed N&B in cells. T.A.J. and S.K. performed and with A.A.-M, A.J.-P., A.L.L., and D.M.P. analyzed genomics data. D.M.P. and G.L.H. supervised cell experiments. D.M.P. supervised A.L.L. and obtained financial support.

All authors critically reviewed and approved the manuscript.

Supplementary data

[Supplementary data](#) is available at NAR online.

Conflict of interest

None declared.

Funding

This work was supported by the Intramural Research Program of the National Institutes of Health (NIH) (ZIA BC 005450), National Cancer Institute (Center for Cancer Research), Ministerio de Ciencia, Innovación y Universidades (MICIU) and Agencia Estatal de Investigación (AEI) (BFU2017-86906-R, PDC2021-121688-100, PID2022-141399-OB-100, CPP2022-009586 to E.E.-P., JDC2022-048702-I to A.J.-P., JDC2023-051138-I to A.A.-M., PID2022-143215OB-I00 to J.F.-R., PID2023-1479660B-I00 to P.P.), Unidad de Excelencia María de Maeztu (CEX2021-001202-M to J.R.-M.), Agència de Gestió d’Ajuts

Universitat de Recerca (AGAUR) - Generalitat de Catalunya (2021SGR01433 to E.E.-P. and 2021SGR00350 to J.R.-M.), Consejo Nacional de Investigaciones Científicas y Técnicas (CONICET) and Agencia Nacional de Promoción de la Investigación, el Desarrollo Tecnológico y la Innovación (ANPCyT) (PICT 2019–0397 to D.M.P.). E.E.-P. also acknowledges the support from the G.E. Carretero Fund. M.N.P.-M acknowledges the Universitat de Barcelona (UB) PREDOC SUB 2020 grant. The Intramural Research Program of the NIH and UB-CRAI funded the open access publication charges for this article.

Data availability

The atomic coordinates and structure factors have been deposited at the Protein Data Bank (PDB) with accession code 9HDF and are publicly available as of the date of publication. The MS/MS proteomics data (*.mzML, *.zhm, *.mzid, *.xlsx, and *.fasta files) have been deposited to the ProteomeXchange Consortium via the PRIDE partner repository with the dataset identifier PXD065782. The Gene Expression profiles are deposited in the Gene Expression Omnibus (GEO) database and the code assigned is GSE282871. All data reported in this paper will be shared by the lead contact upon request. No generative AI or AI-assisted technologies were used at any stage.

Requests for further information or reagents should be directed to and will be fulfilled by the lead contact, Eva Estébanez-Perpiñá (evaestebanez@ub.edu)

All unique/stable reagents generated in this study are available from the lead contact with a completed Materials Transfer Agreement.

References

- Reichardt HM, Kaestner KH, Tuckermann J *et al.* DNA binding of the glucocorticoid receptor is not essential for survival. *Cell* 1998;93:531–41. [https://doi.org/10.1016/S0092-8674\(00\)81183-6](https://doi.org/10.1016/S0092-8674(00)81183-6)
- Oakley RH, Cidlowski JA. The biology of the glucocorticoid receptor: new signaling mechanisms in health and disease. *J Allergy Clin Immunol* 2013;132:1033–44. <https://doi.org/10.1016/j.jaci.2013.09.007>
- Whirlledge S, DeFranco DB. Glucocorticoid signaling in health and disease: insights from tissue-specific GR knockout mice. *Endocrinology* 2018;159:46–64. <https://doi.org/10.1210/en.2017-00728>
- Bledsoe RK, Montana VG, Stanley TB *et al.* Crystal structure of the glucocorticoid receptor ligand binding domain reveals a novel mode of receptor dimerization and coactivator recognition. *Cell* 2002;110:93–105. [https://doi.org/10.1016/S0092-8674\(02\)00817-6](https://doi.org/10.1016/S0092-8674(02)00817-6)
- Evans RM, Mangelsdorf DJ. Nuclear receptors, RXR, and the big bang. *Cell* 2014;157:255–66. <https://doi.org/10.1016/j.cell.2014.03.012>
- Jiménez-Panizo A, Pérez P, Rojas AM *et al.* Non-canonical dimerization of the androgen receptor and other nuclear receptors: implications for human disease. *Endocr Relat Cancer* 2019;26:R479–97. <https://doi.org/10.1530/ERC-19-0132>
- Weikum ER, Knuesel MT, Ortlund EA *et al.* Glucocorticoid receptor control of transcription: precision and plasticity via allostery. *Nat Rev Mol Cell Biol* 2017;18:159–74. <https://doi.org/10.1038/nrm.2016.152>
- Fadel L, Dacic M, Fonda V *et al.* Modulating glucocorticoid receptor actions in physiology and pathology: insights from coregulators. *Pharmacol Ther* 2023;251:108531. <https://doi.org/10.1016/j.pharmthera.2023.108531>
- Auger JP, Zimmermann M, Faas M *et al.* Metabolic rewiring promotes anti-inflammatory effects of glucocorticoids. *Nature* 2024;629:184–92. <https://doi.org/10.1038/s41586-024-07282-7>
- Jiménez-Panizo A, Johnson TA, Wagh K *et al.* Bile acids target an exposed cavity in the glucocorticoid receptor modulating receptor self-assembly, chromatin binding and transcriptional activity. bioRxiv. <https://doi.org/10.1101/2025.05.13.653693>, 16 May 2025, preprint: not peer reviewed.
- Dittmar KD, Demady DR, Stancato LF *et al.* Folding of the glucocorticoid receptor by the heat shock protein (hsp) 90-based chaperone machinery. *J Biol Chem* 1997;272:21213–20. <https://doi.org/10.1074/jbc.272.34.21213>
- Rogatsky I, Wang J-C, Derynck MK *et al.* Target-specific utilization of transcriptional regulatory surfaces by the glucocorticoid receptor. *Proc Natl Acad Sci USA* 2003;100:13845–50. <https://doi.org/10.1073/pnas.2336092100>
- Estébanez-Perpiñá E, Arnold LA, Nguyen P *et al.* A surface on the androgen receptor that allosterically regulates coactivator binding. *Proc Natl Acad Sci USA* 2007;104:16074–9. <https://doi.org/10.1073/pnas.0708036104>
- Buzón V, Carbó LR, Estruch SB *et al.* A conserved surface on the ligand binding domain of nuclear receptors for allosteric control. *Mol Cell Endocrinol* 2012;348:394–402. <https://doi.org/10.1016/j.mce.2011.08.012>
- Jehle K, Cato L, Neeb A *et al.* Coregulator control of androgen receptor action by a novel nuclear receptor-binding motif. *J Biol Chem* 2014;289:8839–51. <https://doi.org/10.1074/jbc.M113.534859>
- Greulich F, Hemmer MC, Rollins DA *et al.* There goes the neighborhood: assembly of transcriptional complexes during the regulation of metabolism and inflammation by the glucocorticoid receptor. *Steroids* 2016;114:7–15. <https://doi.org/10.1016/j.steroids.2016.05.003>
- Noddings CM, Wang RYR, Johnson JL *et al.* Structure of Hsp90–p23–GR reveals the Hsp90 client-remodelling mechanism. *Nature* 2022;601:465–9. <https://doi.org/10.1038/s41586-021-04236-1>
- Escoter-Torres L, Caratti G, Mechtidou A *et al.* Fighting the fire: mechanisms of inflammatory gene regulation by the glucocorticoid receptor. *Front Immunol* 2019;10:1859. <https://doi.org/10.3389/fimmu.2019.01859>
- Syed AP, Greulich F, Ansari SA *et al.* Anti-inflammatory glucocorticoid action: genomic insights and emerging concepts. *Curr Opin Pharmacol* 2020;53:35–44. <https://doi.org/10.1016/j.coph.2020.03.003>
- Meijnsing SH, Puffall MA, So AY *et al.* DNA binding site sequence directs glucocorticoid receptor structure and activity. *Science* 2009;324:407–10. <https://doi.org/10.1126/science.1164265>
- Escoter-Torres L, Greulich F, Quagliarini F *et al.* Anti-inflammatory functions of the glucocorticoid receptor require DNA binding. *Nucleic Acids Res* 2020;48:8393–407. <https://doi.org/10.1093/nar/gkaa565>
- Paakinaho V, Palvimo JJ. Genome-wide crosstalk between steroid receptors in breast and prostate cancers. *Endocr Relat Cancer* 2021;28:R231–50. <https://doi.org/10.1530/ERC-21-0038>
- Green S, Kumar V, Theulaz I *et al.* The N-terminal DNA-binding ‘zinc finger’ of the oestrogen and glucocorticoid receptors determines target gene specificity. *EMBO J* 1988;7:3037–44. <https://doi.org/10.1002/j.1460-2075.1988.tb03168.x>
- Hager GL, Archer TK, Fragoso G *et al.* Influence of chromatin structure on the binding of transcription factors to DNA. *Cold Spring Harb Symp Quant Biol* 1993;58:63–71. <https://doi.org/10.1101/SQB.1993.058.01.010>
- Presman DM, Ganguly S, Schiltz RL *et al.* DNA binding triggers tetramerization of the glucocorticoid receptor in live cells. *Proc Natl Acad Sci USA* 2016;113:8236–41. <https://doi.org/10.1073/pnas.1606774113>

26. Presman DM, Hager GL. More than meets the dimer: what is the quaternary structure of the glucocorticoid receptor? *Transcription* 2017;8:32–9. <https://doi.org/10.1080/21541264.2016.1249045>
27. Fettweis G, Johnson TA, Almeida-Prieto B *et al.* The mineralocorticoid receptor forms higher order oligomers upon DNA binding. *Protein Sci* 2024;33:e4890. <https://doi.org/10.1002/pro.4890>
28. Kino T, Liou S-H, Charmandari E *et al.* Glucocorticoid receptor mutants demonstrate increased motility inside the nucleus of living cells: time of fluorescence recovery after photobleaching (FRAP) is an integrated measure of receptor function. *Mol Med* 2004;10:80–8. <https://doi.org/10.2119/2005-00026.Kino>
29. Meijssing SH, Elbi C, Luecke HF *et al.* The ligand binding domain controls glucocorticoid receptor dynamics independent of ligand release. *Mol Cell Biol* 2007;27:2442–51. <https://doi.org/10.1128/MCB.01570-06>
30. Garcia DA, Fettweis G, Presman DM *et al.* Power-law behavior of transcription factor dynamics at the single-molecule level implies a continuum affinity model. *Nucleic Acids Res* 2021;49:6605–20. <https://doi.org/10.1093/nar/gkab072>
31. Garcia DA, Johnson TA, Presman DM *et al.* An intrinsically disordered region-mediated confinement state contributes to the dynamics and function of transcription factors. *Mol Cell* 2021;81:1484–98. <https://doi.org/10.1016/j.molcel.2021.01.013>
32. Wagh K, Ishikawa M, Garcia DA *et al.* Mechanical regulation of transcription: recent advances. *Trends Cell Biol* 2021;31:457–72. <https://doi.org/10.1016/j.tcb.2021.02.008>
33. Wagh K, Stavreva DA, Upadhyaya A *et al.* Transcription factor dynamics: one molecule at a time. *Annu Rev Cell Dev Biol* 2023;39:277–305. <https://doi.org/10.1146/annurev-cellbio-022823-013847>
34. Wagh K, Stavreva DA, Jensen RAM *et al.* Dynamic switching of transcriptional regulators through two distinct low-mobility chromatin states. *Sci Adv* 2023;9:1–19. <https://doi.org/10.1126/sciadv.ade1122>
35. Wagh K, Stavreva DA, Hager GL. Transcription dynamics and genome organization in the mammalian nucleus: recent advances. *Mol Cell* 2024;85:208–24. <https://doi.org/10.1016/j.molcel.2024.09.022>
36. Johnson TA, Fettweis G, Wagh K *et al.* The glucocorticoid receptor potentiates aldosterone-induced transcription by the mineralocorticoid receptor. *Proc Natl Acad Sci USA* 2024;121:e2413737121. <https://doi.org/10.1073/pnas.2413737121>
37. Vottero A, Kino T, Combe H *et al.* A novel, C-terminal dominant negative mutation of the GR causes familial glucocorticoid resistance through abnormal interactions with p160 steroid receptor coactivators. *J Clin Endocrinol Metab* 2002;87:2658–67. <https://doi.org/10.1210/jcem.87.6.8520>
38. Chrousos G. Q&A: primary generalized glucocorticoid resistance. *BMC Med* 2011;9:27. <https://doi.org/10.1186/1741-7015-9-27>
39. Nicolaidis NC, Skyrla E, Vlachakis D *et al.* Functional characterization of the hGR α T556I causing Chrousos syndrome. *Eur J Clin Investigation* 2016;46:42–9. <https://doi.org/10.1111/eci.12563>
40. Molnár Á, Patócs A, Likó I *et al.* An unexpected, mild phenotype of glucocorticoid resistance associated with glucocorticoid receptor gene mutation case report and review of the literature. *BMC Med Genet* 2018;19:37. <https://doi.org/10.1186/s12881-018-0552-6>
41. Charmandari E, Kino T, Chrousos GP. Primary generalized familial and sporadic glucocorticoid resistance (Chrousos syndrome) and hypersensitivity. *Endocr Dev* 2013;24:67–85. <https://doi.org/10.1159/000342505>
42. Kino T, Chrousos G. Glucocorticoid and mineralocorticoid resistance/hypersensitivity syndromes. *J Endocrinol* 2001;169:437–45. <https://doi.org/10.1677/joe.0.1690437>
43. Kadmiel M, Cidlowski JA. Glucocorticoid receptor signaling in health and disease. *Trends Pharmacol Sci* 2013;34:518–30. <https://doi.org/10.1016/j.tips.2013.07.003>
44. Carson MW, Luz JG, Suen C *et al.* Glucocorticoid receptor modulators informed by crystallography lead to a new rationale for receptor selectivity, function, and implications for structure-based design. *J Med Chem* 2014;57:849–60. <https://doi.org/10.1021/jm401616g>
45. Cain DW, Cidlowski JA. Specificity and sensitivity of glucocorticoid signaling in health and disease. *Best Pract Res Clin Endocrinol Metab* 2015;29:545–56. <https://doi.org/10.1016/j.beem.2015.04.007>
46. Giroud M, Tsokanos FF, Caratti G *et al.* HAND2 is a novel obesity-linked adipogenic transcription factor regulated by glucocorticoid signalling. *Diabetologia* 2021;64:1850–65. <https://doi.org/10.1007/s00125-021-05470-y>
47. Caratti G, Stifel U, Caratti B *et al.* Glucocorticoid activation of anti-inflammatory macrophages protects against insulin resistance. *Nat Commun* 2023;14:2271. <https://doi.org/10.1038/s41467-023-37831-z>
48. Prekovic S, Chalkiadakis T, Roest M *et al.* Luminal breast cancer identity is determined by loss of glucocorticoid receptor activity. *EMBO Mol Med* 2023;15:e17737. <https://doi.org/10.15252/emmm.202317737>
49. Clarisse D, Van Moortel L, Van Leene C *et al.* Glucocorticoid receptor signaling: intricacies and therapeutic opportunities. *Trends Biochem Sci* 2024;49:431–44. <https://doi.org/10.1016/j.tibs.2024.01.012>
50. Luisi BF, Xu WX, Otwinowski Z *et al.* Crystallographic analysis of the interaction of the glucocorticoid receptor with DNA. *Nature* 1991;352:497–505. <https://doi.org/10.1038/352497a0>
51. Hudson WH, Youn C, Ortlund EA. The structural basis of direct glucocorticoid-mediated transrepression. *Nat Struct Mol Biol* 2013;20:53–8. <https://doi.org/10.1038/nsmb.2456>
52. Frank F, Okafor CD, Ortlund EA. The first crystal structure of a DNA-free nuclear receptor DNA binding domain sheds light on DNA-driven allostery in the glucocorticoid receptor. *Sci Rep* 2018;8:13497. <https://doi.org/10.1038/s41598-018-31812-9>
53. Kauppi B, Jakob C, Färnegårdh M *et al.* The three-dimensional structures of antagonistic and agonistic forms of the glucocorticoid receptor ligand-binding domain: RU-486 induces a transconformation that leads to active antagonism. *J Biol Chem* 2003;278:22748–54. <https://doi.org/10.1074/jbc.M212711200>
54. Jiménez-Panizo A, Alegre-Martí A, Tettey TT *et al.* The multivalency of the glucocorticoid receptor ligand-binding domain explains its manifold physiological activities. *Nucleic Acids Res* 2022;50:13063–82. <https://doi.org/10.1093/nar/gkac1119>
55. Postel S, Wissler L, Johansson CA *et al.* Quaternary glucocorticoid receptor structure highlights allosteric interdomain communication. *Nat Struct Mol Biol* 2023;30:286–95. <https://doi.org/10.1038/s41594-022-00914-4>
56. Paakinaho V, Kaikkonen S, Makkonen H *et al.* SUMOylation regulates the chromatin occupancy and anti-proliferative gene programs of glucocorticoid receptor. *Nucleic Acids Res* 2014;42:1575–92. <https://doi.org/10.1093/nar/gkt1033>
57. Iyer-Bierhoff A, Wiczorek M, Peter SM *et al.* Acetylation-induced proteasomal degradation of the activated glucocorticoid receptor limits hormonal signaling. *Iscience* 2024;27:108943. <https://doi.org/10.1016/j.isci.2024.108943>
58. Juanhuix J, Gil-Ortiz F, Cuní G *et al.* Developments in optics and performance at BL13-XALOC, the macromolecular crystallography beamline at the Alba Synchrotron. *J Synchrotron Rad* 2014;21:679–89. <https://doi.org/10.1107/S160057751400825X>
59. Broennimann C, Eikenberry EF, Henrich B *et al.* The PILATUS 1M detector. *J Synchrotron Rad* 2006;13:120–30. <https://doi.org/10.1107/S0909049505038665>

60. Agirre J, Atanasova M, Bagdonas H *et al.* The CCP4 suite: integrative software for macromolecular crystallography. *Acta Crystallogr D Struct Biol* 2023;79:449–61. <https://doi.org/10.1107/S2059798323003595>
61. Vagin A, Teplyakov A. Molecular replacement with MOLREP. *Acta Crystallogr D Biol Crystallogr* 2010;66:22–5. <https://doi.org/10.1107/S0907444909042589>
62. Murshudov GN, Skubák P, Lebedev AA *et al.* REFMAC 5 for the refinement of macromolecular crystal structures. *Acta Crystallogr D Biol Crystallogr* 2011;67:355–67. <https://doi.org/10.1107/S0907444911001314>
63. Matthews BW. Solvent content of protein crystals. *J Mol Biol* 1968;33:491–7. [https://doi.org/10.1016/0022-2836\(68\)90205-2](https://doi.org/10.1016/0022-2836(68)90205-2)
64. Krissinel E, Henrick K. Inference of macromolecular assemblies from crystalline state. *J Mol Biol* 2007;372:774–97. <https://doi.org/10.1016/j.jmb.2007.05.022>
65. Davis IW, Leaver-Fay A, Chen VB *et al.* MolProbity: all-atom contacts and structure validation for proteins and nucleic acids. *Nucleic Acids Res* 2007;35:W375–83. <https://doi.org/10.1093/nar/gkm216>
66. McGuffin LJ, Alharbi SMA. ModFOLD9: a web server for independent estimates of 3D protein model quality. *J Mol Biol* 2024;436:168531. <https://doi.org/10.1016/j.jmb.2024.168531>
67. Alegre-Martí A, Jiménez-Panizo A, Martínez-Tébar A *et al.* A hotspot for posttranslational modifications on the androgen receptor dimer interface drives pathology and anti-androgen resistance. *Sci Adv* 2023;9:6–7. <https://doi.org/10.1126/sciadv.ade2175>
68. Götze M, Pettelkau J, Fritzsche R *et al.* Automated assignment of MS/MS cleavable cross-links in protein 3D-structure analysis. *J Am Soc Mass Spectrom* 2015;26:83–97. <https://doi.org/10.1007/s13361-014-1001-1>
69. Iacobucci C, Götze M, Ihling CH *et al.* A cross-linking/mass spectrometry workflow based on MS-cleavable cross-linkers and the MeroX software for studying protein structures and protein–protein interactions. *Nat Protoc* 2018;13:2864–89. <https://doi.org/10.1038/s41596-018-0068-8>
70. Mendes ML, Fischer L, Chen ZA *et al.* An integrated workflow for crosslinking mass spectrometry. *Mol Syst Biol* 2019;15:e8994. <https://doi.org/10.15252/msb.20198994>
71. Liu F, Rijkers DTS, Post H *et al.* Proteome-wide profiling of protein assemblies by cross-linking mass spectrometry. *Nat Methods* 2015;12:1179–84. <https://doi.org/10.1038/nmeth.3603>
72. Paakinaho V, Johnson TA, Presman DM *et al.* Glucocorticoid receptor quaternary structure drives chromatin occupancy and transcriptional outcome. *Genome Res* 2019;29:1223–34. <https://doi.org/10.1101/gr.244814.118>
73. Johnson TA, Paakinaho V, Kim S *et al.* Genome-wide binding potential and regulatory activity of the glucocorticoid receptor's monomeric and dimeric forms. *Nat Commun* 2021;12:1987. <https://doi.org/10.1038/s41467-021-22234-9>
74. Paakinaho V, Presman DM, Ball DA *et al.* Single-molecule analysis of steroid receptor and cofactor action in living cells. *Nat Commun* 2017;8:15896. <https://doi.org/10.1038/ncomms15896>
75. Mikuni S, Tamura M, Kinjo M. Analysis of intranuclear binding process of glucocorticoid receptor using fluorescence correlation spectroscopy. *FEBS Lett* 2007;581:389–93. <https://doi.org/10.1016/j.febslet.2006.12.038>
76. Digman MA, Dalal R, Horwitz AF *et al.* Mapping the number of molecules and brightness in the laser scanning microscope. *Biophys J* 2008;94:2320–32. <https://doi.org/10.1529/biophysj.107.114645>
77. McNally JG, Müller WG, Walker D *et al.* The glucocorticoid receptor: rapid exchange with regulatory sites in living cells. *Science* 2000;287:1262–5. <https://doi.org/10.1126/science.287.5456.1262>
78. Dobin A, Davis CA, Schlesinger F *et al.* STAR: ultrafast universal RNA-seq aligner. *Bioinformatics* 2013;29:15–21. <https://doi.org/10.1093/bioinformatics/bts635>
79. Love MI, Huber W, Anders S. Moderated estimation of fold change and dispersion for RNA-seq data with DESeq2. *Genome Biol* 2014;15:550. <https://doi.org/10.1186/s13059-014-0550-8>
80. Cheng TMK, Blundell TL, Fernandez-Recio J. PyDock: electrostatics and desolvation for effective scoring of rigid-body protein–protein docking. *Proteins* 2007;68:503–15. <https://doi.org/10.1002/prot.21419>
81. Canutescu AA, Shelenkov AA, Dunbrack RL. A graph-theory algorithm for rapid protein side-chain prediction. *Protein Science* 2003;12:2001–14. <https://doi.org/10.1110/ps.03154503>
82. Gabb HA, Jackson RM, Sternberg MJE. Modelling protein docking using shape complementarity, electrostatics and biochemical information. *J Mol Biol* 1997;272:106–20. <https://doi.org/10.1006/jmbi.1997.1203>
83. Chen R, Li L, Weng Z. ZDOCK: an initial-stage protein-docking algorithm. *Proteins* 2003;52:80–7. <https://doi.org/10.1002/prot.10389>
84. Grosdidier S, Fernández-Recio J. Identification of hot-spot residues in protein–protein interactions by computational docking. *BMC Bioinformatics* 2008;9:447. <https://doi.org/10.1186/1471-2105-9-447>
85. Schrödinger. Maestro. 2025. <https://www.schrodinger.com/platform/products/maestro/>
86. Wang J, Wolf RM, Caldwell JW *et al.* Development and testing of a general amber force field. *J Comput Chem* 2004;25:1157–74. <https://doi.org/10.1002/jcc.20035>
87. Bayly CI, Cieplak P, Cornell W *et al.* A well-behaved electrostatic potential based method using charge restraints for deriving atomic charges: the RESP model. *J Phys Chem* 1993;97:10269–80. <https://doi.org/10.1021/j100142a004>
88. Case DA, Aktulga HM, Belfon K *et al.* Amber 2022.2022.
89. Tian C, Kasavajhala K, Belfon KAA *et al.* ff19SB: amino-acid-specific protein backbone parameters trained against quantum mechanics energy surfaces in solution. *J Chem Theory Comput* 2020;16:528–52. <https://doi.org/10.1021/acs.jctc.9b00591>
90. Izadi S, Anandakrishnan R, Onufriev AV. Building water models: a different approach. *J Phys Chem Lett* 2014;5:3863–71. <https://doi.org/10.1021/jz501780a>
91. Darden T, York D, Pedersen L. Particle mesh ewald: an N·log(N) method for Ewald sums in large systems. *J Chem Phys* 1993;98:10089–92. <https://doi.org/10.1063/1.464397>
92. Hopkins CW, Le Grand S, Walker RC *et al.* Long-time-step molecular dynamics through hydrogen mass repartitioning. *J Chem Theory Comput* 2015;11:1864–74. <https://doi.org/10.1021/ct5010406>
93. Ryckaert J-P, Ciccotti G, Berendsen HJC. Numerical integration of the cartesian equations of motion of a system with constraints: molecular dynamics of n-alkanes. *J Comput Phys* 1977;23:327–41. [https://doi.org/10.1016/0021-9991\(77\)90098-5](https://doi.org/10.1016/0021-9991(77)90098-5)
94. Perez JJ, Tomas MS, Rubio-Martinez J. Assessment of the sampling performance of multiple-copy dynamics versus a unique trajectory. *J Chem Inf Model* 2016;56:1950–62. <https://doi.org/10.1021/acs.jcim.6b00347>
95. Rokach L, Maimon O. Clustering methods. In *Data Mining and Knowledge Discovery Handbook*. Boston, MA, USA: Springer, 2005. 321–52. <https://doi.org/10.1007/b107408>
96. Roe DR, Cheatham TE. PTRAJ and CPPTRAJ: software for processing and analysis of molecular dynamics trajectory data. *J Chem Theory Comput* 2013;9:3084–95. <https://doi.org/10.1021/ct400341p>
97. Vatansever S, Erman B, Gümüş ZH. Oncogenic G12D mutation alters local conformations and dynamics of K-Ras. *Sci Rep* 2019;9:11730. <https://doi.org/10.1038/s41598-019-48029-z>
98. Atilgan AR, Akan P, Baysal C. Small-world communication of residues and significance for protein dynamics. *Biophys J* 2004;86:85–91. [https://doi.org/10.1016/S0006-3495\(04\)74086-2](https://doi.org/10.1016/S0006-3495(04)74086-2)

99. Schrödinger L. The PyMOL molecular graphics system. <https://www.pymol.org/>
100. Seitz T, Thoma R, Schoch GA *et al.* Enhancing the stability and solubility of the glucocorticoid receptor ligand-binding domain by high-throughput library screening. *J Mol Biol* 2010;403:562–77. <https://doi.org/10.1016/j.jmb.2010.08.048>
101. Álvarez LD, Martí MA, Veleiro AS *et al.* Exploring the molecular basis of action of the passive antiglucocorticoid 21-hydroxy-6, 19-epoxyprogesterone. *J Med Chem* 2008;51:1352–60. <https://doi.org/10.1021/jm800007w>
102. Laulhé M, Kuhn E, Bouligand J *et al.* A novel mutation in the NR3C1 gene associated with reversible glucocorticoid resistance. *Eur J Endocrinol* 2024;190:284–95. <https://doi.org/10.1093/ejendo/lvae031>
103. Ma B, Elkayam T, Wolfson H *et al.* Protein–protein interactions: structurally conserved residues distinguish between binding sites and exposed protein surfaces. *Proc Natl Acad Sci USA* 2003;100:5772–7. <https://doi.org/10.1073/pnas.1030237100>
104. Dey S, Pal A, Chakrabarti P *et al.* The subunit interfaces of weakly associated homodimeric proteins. *J Mol Biol* 2010;398:146–60. <https://doi.org/10.1016/j.jmb.2010.02.020>
105. Chakravarty D, Janin J, Robert CH *et al.* Changes in protein structure at the interface accompanying complex formation. *IUCrJ* 2015;2:643–52. <https://doi.org/10.1107/S2052252515015250>
106. He Y, Yi W, Suino-Powell K *et al.* Structures and mechanism for the design of highly potent glucocorticoids. *Cell Res* 2014;24:713–26. <https://doi.org/10.1038/cr.2014.52>
107. Biggadike K, Bledsoe RK, Hassell AM *et al.* X-ray crystal structure of the novel enhanced-affinity glucocorticoid agonist fluticasone furoate in the glucocorticoid receptor–ligand binding domain. *J Med Chem* 2008;51:3349–52. <https://doi.org/10.1021/jm800279t>
108. Madauss KP, Bledsoe RK, Mclay I *et al.* The first X-ray crystal structure of the glucocorticoid receptor bound to a non-steroidal agonist. *Bioorganic Med Chem Lett* 2008;18:6097–9. <https://doi.org/10.1016/j.bmcl.2008.10.021>
109. Biggadike K, Bledsoe RK, Coe DM *et al.* Design and x-ray crystal structures of high-potency nonsteroidal glucocorticoid agonists exploiting a novel binding site on the receptor. *Proc Natl Acad Sci USA* 2009;106:18114–9. <https://doi.org/10.1073/pnas.0909125106>
110. Presman DM, Ogara MF, Stortz M *et al.* Live cell imaging unveils multiple domain requirements for *in vivo* dimerization of the glucocorticoid receptor. *PLoS Biol* 2014;12:e1001813. <https://doi.org/10.1371/journal.pbio.1001813>
111. Lee S-J, Shizu R, Negishi M. Glucocorticoid receptor dimerization in the cytoplasm might be essential for nuclear localization. *Biochem Biophysical Research Communications* 2021;553:154–9. <https://doi.org/10.1016/j.bbrc.2021.03.071>
112. Chandra V, Huang P, Potluri N *et al.* Multidomain integration in the structure of the HNF-4 α nuclear receptor complex. *Nature* 2013;495:394–8. <https://doi.org/10.1038/nature11966>
113. Freeman BC, Yamamoto KR. Disassembly of transcriptional regulatory complexes by molecular chaperones. *Science* 2002;296:2232–5. <https://doi.org/10.1126/science.1073051>
114. Zhu HJ, Dai YF, Wang O *et al.* Generalized glucocorticoid resistance accompanied with an adrenocortical adenoma and caused by a novel point mutation of human glucocorticoid receptor gene. *Chin Med J (Engl)* 2011;124:551–5. <https://doi.org/10.3760/cma.j.issn.0366-6999.2011.04.013>
115. Malchoff DM, Brufsky A, Reardon G *et al.* A mutation of the glucocorticoid receptor in primary cortisol resistance. *J Clin Invest* 1993;91:1918–25. <https://doi.org/10.1172/JCI116410>
116. Charmandari E, Raji A, Kino T *et al.* A novel point mutation in the ligand-binding domain (LBD) of the human glucocorticoid receptor (hGR) causing generalized glucocorticoid resistance: the importance of the C terminus of hGR LBD in conferring transactivational activity. *J Clin Endocrinol Metab* 2005;90:3696–705. <https://doi.org/10.1210/jc.2004-1920>
117. Charmandari E, Kino T, Ichijo T *et al.* A novel point mutation in helix 11 of the ligand-binding domain of the human glucocorticoid receptor gene causing generalized glucocorticoid resistance. *J Clin Endocrinol Metab* 2007;92:3986–90. <https://doi.org/10.1210/jc.2006-2830>
118. Nicolaides NC, Roberts ML, Kino T *et al.* A novel point mutation of the human glucocorticoid receptor gene causes primary generalized glucocorticoid resistance through impaired interaction with the LXXLL motif of the p160 coactivators: dissociation of the transactivating and transrepressive activities. *J Clin Endocrinol Metab* 2014;99:902–7. <https://doi.org/10.1210/jc.2013-3005>
119. Kaziales A, Rührnößl F, Richter K. Glucocorticoid resistance conferring mutation in the C-terminus of GR alters the receptor conformational dynamics. *Sci Rep* 2021;11:12515. <https://doi.org/10.1038/s41598-021-92039-9>
120. Tian S, Poukka H, Palvimo JJ *et al.* Small ubiquitin-related modifier-1 (SUMO-1) modification of the glucocorticoid receptor. *Biochem J* 2002;367:907–11. <https://doi.org/10.1042/bj20021085>
121. Druker J, Liberman AC, Antunica-Noguerol M *et al.* RSUME enhances glucocorticoid receptor SUMOylation and transcriptional activity. *Mol Cell Biol* 2013;33:2116–27. <https://doi.org/10.1128/MCB.01470-12>
122. Liu X, Wang Y, Ortlund EA. First high-resolution crystal structures of the glucocorticoid receptor ligand-binding domain–peroxisome proliferator-activated γ coactivator 1- α complex with endogenous and synthetic glucocorticoids. *Mol Pharmacol* 2019;96:408–17. <https://doi.org/10.1124/mol.119.116806>
123. Bianchetti L, Wassmer B, Defosset A *et al.* Alternative dimerization interfaces in the glucocorticoid receptor- α ligand binding domain. *Biochim Biophys Acta* 2018;1862:1810–25. <https://doi.org/10.1016/j.bbagen.2018.04.022>
124. Cunha Lima ST, Nguyen N-H, Togashi M *et al.* Differential effects of TR ligands on hormone dissociation rates: evidence for multiple ligand entry/exit pathways. *J Steroid Biochem Mol Biol* 2009;117:125–31. <https://doi.org/10.1016/j.jsbmb.2009.08.003>
125. Fischer A, Smieško M. Ligand pathways in nuclear receptors. *J Chem Inf Model* 2019;59:3100–9. <https://doi.org/10.1021/acs.jcim.9b00360>
126. Frank F, Liu X, Ortlund EA. Glucocorticoid receptor condensates link DNA-dependent receptor dimerization and transcriptional transactivation. *Proc Natl Acad Sci USA* 2021;118:e2024685118. <https://doi.org/10.1073/pnas.2024685118>
127. Hakim O, John S, Ling JQ *et al.* Glucocorticoid receptor activation of the Ciz1-Lcn2 locus by long range interactions. *J Biol Chem* 2009;284:6048–52. <https://doi.org/10.1074/jbc.C800212200>
128. Hakim O, Sung MH, Voss TC *et al.* Diverse gene reprogramming events occur in the same spatial clusters of distal regulatory elements. *Genome Res* 2011;21:697–706. <https://doi.org/10.1101/gr.111153.110>
129. Stavreva DA, Coulon A, Baek S *et al.* Dynamics of chromatin accessibility and long-range interactions in response to glucocorticoid pulsing. *Genome Res* 2015;25:845–57. <https://doi.org/10.1101/gr.184168.114>
130. Tettey TT, Rinaldi L, Hager GL. Long-range gene regulation in hormone-dependent cancer. *Nat Rev Cancer* 2023;23:657–72. <https://doi.org/10.1038/s41568-023-00603-4>
131. Nadal M, Prekovic S, Gallastegui N *et al.* Structure of the homodimeric androgen receptor ligand-binding domain. *Nat Commun* 2017;8:14388. <https://doi.org/10.1038/ncomms14388>
132. Alvarez de la Rosa D, Ramos-Hernández Z, Weller-Pérez J *et al.* The impact of mineralocorticoid and glucocorticoid receptor interaction on corticosteroid transcriptional outcomes. *Mol Cell*

Endocrinol 2024;594:112389.

<https://doi.org/10.1016/j.mce.2024.112389>

133. Levy N, Eiler S, Pradeau-Aubretton K *et al.* Production of unstable proteins through the formation of stable core complexes. *Nat Commun* 2016;7:10932. <https://doi.org/10.1038/ncomms10932>
134. Murani E, Reyer H, Ponsuksili S *et al.* A substitution in the ligand binding domain of the porcine glucocorticoid receptor affects activity of the adrenal gland. *PLoS One* 2012;7:e45518. <https://doi.org/10.1371/journal.pone.0045518>
135. Reyer H, Ponsuksili S, Kanitz E *et al.* A natural mutation in helix 5 of the ligand binding domain of glucocorticoid receptor enhances receptor-ligand interaction. *PLoS One* 2016;11:e0164628. <https://doi.org/10.1371/journal.pone.0164628>